Drivers of organic carbon distribution and accumulation in the northern Barents Sea

Thaise Ricardo de Freitas [a,*], Silvia Hess [a], Paul E. Renaud [b,c], Peter Appleby [d], Elisabeth Alve [a]

[a] Department of Geosciences, University of Oslo, Oslo, Norway
[b] Akvaplan-niva, Fram Centre for Climate and the Environment, Tromsø, Norway
[c] University Centre on Svalbard, Svalbard, Norway
[d] Environmental Radioactivity Research Centre, University of Liverpool, Liverpool, UK

ABSTRACT

Sedimentary properties and accumulation rates on the continental shelf and in the deep sea reflect temporal oceanographic, biological and chemical processes occurring in the water column and the sediment surface. We used the radionuclides ^{210}Pb, ^{226}Ra, and ^{137}Cs activities to estimate sedimentation rates during the last century at nine stations in the northern Barents Sea region. Elemental (C, N) and stable isotopic composition (δ^{13}C, δ^{15}N) were also analysed from the nine stations sampled in August 2018, and, for five other stations sampled in August and December 2019, and in March and May 2021. Sediment accumulation rates varied between 130 and 1 410 g m^{-2} y^{-1}. The < 63 μm normalized total organic carbon (TOC$_{63}$) and the total nitrogen from the sediment surface varied between 0.90–2.56 % and 0.13–0.33 %, respectively. Ice-free shelf stations had higher TOC$_{63}$ and possibly fresher organic matter (high δ^{13}C, low δ^{15}N) than ice-covered more northern stations. The opposite trend was observed for total inorganic carbon. We found that these trends in biogeochemical parameters were spatially structured by the winter sea ice concentration and biological production differences, and exhibited a south-north separation of the Polar Front region. The low and stable organic carbon accumulation rate (1.7–13.4 g C$_{org}$ m^{-2} y^{-1}; AR$_{toc}$) is a function of slow sedimentation rates, and high degradation and residence time in the water column and at the sediment–water interface. Overall, the AR$_{toc}$ has been stable for the past 100 years, with a slight increase from the early 1970s to the present at the shelf and slope stations. Our results highlight that spatial scales of variability of the studied sedimentary parameters are linked to spatial patterns of important environmental variables (e.g., chlorophyll-a, sea ice concentration) in the region. In contrast, no seasonal differences were observed in the sediment parameters of revisited stations, and the dated sediment geochemical profiles did not exhibit substantial longer-term variation. This means that climate-induced changes in variables that modify the sedimentary geochemistry of the environment may affect benthic community activity and structure before leaving a record in AR$_{toc}$.

1. Introduction

The Arctic carbon cycle and the processes determining organic carbon flux and accumulation in marine sediments play important roles in the global climate system (Lannuzel et al., 2020). In general, temperate and Arctic seas act as carbon sinks (Laruelle et al., 2014; Fennel et al., 2019). Continental shelves account for a significant proportion of organic carbon storage in the marine realm (Bauer et al., 2013) but with high spatial and temporal variability (Laruelle et al., 2018). Many of these shelf seas are under constant anthropogenic disturbance due to their high economic exploitation and exploration of mining, dredging,

and trawling activities. These disturbances are also relevant for highly productive Arctic shelves, where multiple mechanisms, such as CO$_2$ uptake, biological production and respiration, and sediment accretion control carbon export and storage in sediments (Yasunaka et al., 2018; Wiedmann et al., 2020).

The most pronounced declines in the Arctic annual sea ice extent and thickness are occurring in the Barents Sea (Årthun et al., 2012). On this highly productive shelf, the seasonal and interannual dynamics of both inflowing warm and saline Atlantic Water from the Norwegian Current (Årthun et al., 2012) and freshwater discharge (Lind et al., 2018) directly influence the amount of ice produced during wintertime. In the

northern Barents Sea, where warm and saline Atlantic waters meet the Arctic domain, freshwater enters as sea-ice, keeping the region cold, stratified and seasonally ice-covered. In a warming climate, sea-ice becomes thinner, sparse and mobile, which causes the border of the Arctic domain to retreat and the Atlantic Water to advance, gradually shrinking the area where ice forms in winter (Lind et al., 2018). While this domain division results from differences in the physical environment it also drives contrasts in biogeochemical gradients and biological processes (Faust et al., 2020).

As climatic variation determines the ice distribution, it also regulates vertical mixing and water mass stratification, which help determine the rate and timing of primary production. The northern Barents Sea's primary productivity is composed of both pelagic and ice algal production. The latter is initiated before the pelagic production and relies on light that penetrates the ice (Falk-Petersen et al., 2000). Reductions in sea-ice thickness and coverage will alter the current primary production regime, with consequences for the secondary producers and consumers (Lannuzel et al., 2020). Whereas nutrient availability is more relevant to sustain and set the upper limit of phytoplankton growth, water column stability is often an important factor in initiating the bloom (Harrison and Cota, 1991; Strass and Niithig, 1996), and imposes a barrier to nutrient resupply once depleted. Thus, changes in bloom pulses or vertical water-mass structure derived from climatic change can potentially alter the amount and quality of the organic matter reaching the seafloor, with consequences for the carbon cycle in the water column, vertical carbon flux and benthic ecosystem functioning (Stevenson and Abbott, 2019; Wiedmann et al., 2020).

Most of the organic carbon available in the Barents Sea sediments has been previously described as of marine origin (Knies and Martinez, 2009). The low terrestrial contribution is often associated with sediment-laden sea ice, river inflow and recirculation (Nürnberg et al., 1995; Rachold et al., 2004). As a consequence, sea ice reduction, enhanced Atlantic Water inflow, and associated changes in biological production will likely modify the future distribution and accumulation of organic carbon in Barents Sea sediments, more so than increased sediment runoff from rivers and coastal erosion (Rachold et al., 2004). Modern sediment accumulation rates give valuable information about processes occurring in the water column over different time scales (Sternberg et al., 2001; Zaborska et al., 2008; Maiti et al., 2010; Pathirana et al., 2015), and despite these recent research efforts, more studies covering sedimentation and carbon accumulation processes in the northern Barents Sea would be valuable. In this study, we extend previous assessments of the distribution of modern sediment properties and organic carbon accumulation in the northern Barents Sea. For this purpose, sediment elemental (C, N) and stable isotopic composition (δ^{13}C, δ^{15}N) were investigated in different sections of a shelf-to-basin transect with distinct geomorphological, geochemical, and hydrographic features. We examined the recent temporal variation of these properties in radiometrically dated short sediment cores covering the last century. We also revisited stations along the sampled transect to determine whether seasonal changes in environmental drivers are evident in sediment properties. Based on the above, our objective is to understand how these properties are linked to the spatial and temporal patterns of environmental variables (e.g., water depth, sea ice concentration). This study contributes to a better understanding of current and future biogeochemical processes and their scaling properties in this vulnerable environment upon climate warming.

2. Materials and methods

2.1. Study area

The Barents Sea is the largest Arctic marginal shelf sea (Fig. 1). Due to its close connection with the Norwegian Sea and the Arctic Ocean, it is a key region for mixing warmer and more saline water from the southern Atlantic Water (AW) and colder and fresher northern Polar Water (PW)

(Loeng, 1991; Pfirman et al., 1994; Lind and Ingvaldsen, 2012). The Polar Front (PF) is a water mass boundary region between the AW and PW, dividing the Arctic and Atlantic domains (Loeng, 1991). The AW enters the Barents Sea via two main pathways. In the south-western region, the AW flows northwards via the Hopendypet (HD) and divides into smaller branches near Storbanken (SB) (Loeng, 1991). In the northern region, a branch of AW flows along the Svalbard shelf as a boundary current, turns eastwards, and enters the Barents Sea from the North via Kvitøyrenna (KR) and the Franz-Victoria Trough (Pfirman et al., 1994; Lind and Ingvaldsen, 2012). This AW branch is cooled and freshened as it continues southwards via Erik Eriksenstretet (ES) and Kong Karls Trough (KT) towards Olgastretet (OS), where it recirculates before exiting through the Franz Victoria Trough or flowing eastwards (Lind and Ingvaldsen, 2012; Athanase et al., 2021).

With a mean depth of 200 m and a slope between 400 and 2000 m, the highly irregular bottom topography of the Barents Sea drives the general circulation, while the water masses' vertical distribution is influenced by the ocean's interaction with the atmosphere and the sea ice (Loeng, 1991). Water flowing over shallow regions increases density in winter through heat loss and brine rejection amid sea ice formation, while surface water loses density in summer by warming and addition of sea-ice meltwater and river runoff (Midttun, 1985; Loeng, 1991; Pfirman et al., 1994). These processes, in turn, affect particle transport in the area. In the northern Barents Sea, glacial meltwater is prominent in delivering sediment (Dowdeswell et al., 1998) and may be responsible for up to 30 % of modern sedimentation in the region (Elverhøi et al., 1989). Generally, the bedrock is covered by a thin (<10 m) layer of unconsolidated sediment of Quaternary age overlain by a thin layer (0.2 to 1.0 m) of recent marine mud (Elverhøi et al., 1989).

2.2. Sampling design and data collection

Sediment sampling was performed during five expeditions of the Nansen Legacy Project (arvenetternansen.com) onboard R/V Kronprins Haakon − September 2018 (Nansen Paleo cruise − NPAL), August 2019 (Seasonal Study Q3 − SSQ3), December 2019 (SSQ4), March 2021 (SSQ1), and April 2021 (SSQ2), between 75–83 °N and 24–34 °E (Fig. 1). During all seasons, Atlantic water dominated the station south of the Polar Front (P1), while Polar Water characterized the water column of stations P2 to P4 (Fig. 1). North of the shelf break (P6 and P7), cold Polar Water was present as well as Atlantic water in deeper layers (Jones et al., 2023). Station P1 is ice-free year-round (Figure S1). During sampling, the stations A and B were ice-free, P2–NPAL14 were seasonally ice-covered and P6-NPAL17 were ice-covered (Fig. 1). More information about sampling stations ice coverage can be found in the Supplementary Figure S1.

Sediment cores (40 cm long, 10 cm diameter) were retrieved at nine NPAL stations (NPAL04 to NPAL19) with a four-tube multi-corer, immediately sliced into 1 cm layers, and subsamples were frozen (−20 °C) on board. All NPAL sediment slices were freeze-dried in the laboratory and subsampled for radionuclide analyses, grain size and geochemical analyses. Additionally, twenty-eight short sediment cores (6 cm length x 5 cm diameter) were subsampled from giant box corer deployments at six stations (P1 to SICE4; 3 replicates) during the four seasonal cruises (SSQ1 to SSQ4). All sediment cores were immediately sliced into 1 cm layers and subsamples were directly frozen on board (−20 °C). All subsamples from SSQ1 to SSQ4 were freeze-dried in the laboratory sampled for geochemical analyses. Sediment samples from stations A and B (Fig. 1) were subsampled from a combi-grab in August 2019. The geochemical data of these short sediment cores were incorporated to expand the spatial distribution of organic carbon (OC) content and aid in interpretation. Details of the analyses performed in each sediment core are available in Table S1.

The environmental data used for statistical analyses in this study are sea surface and bottom temperature (SST, SBT), sea surface and bottom salinity (SSS, SBS), sea surface and bottom dissolved oxygen (SSO, SBO),
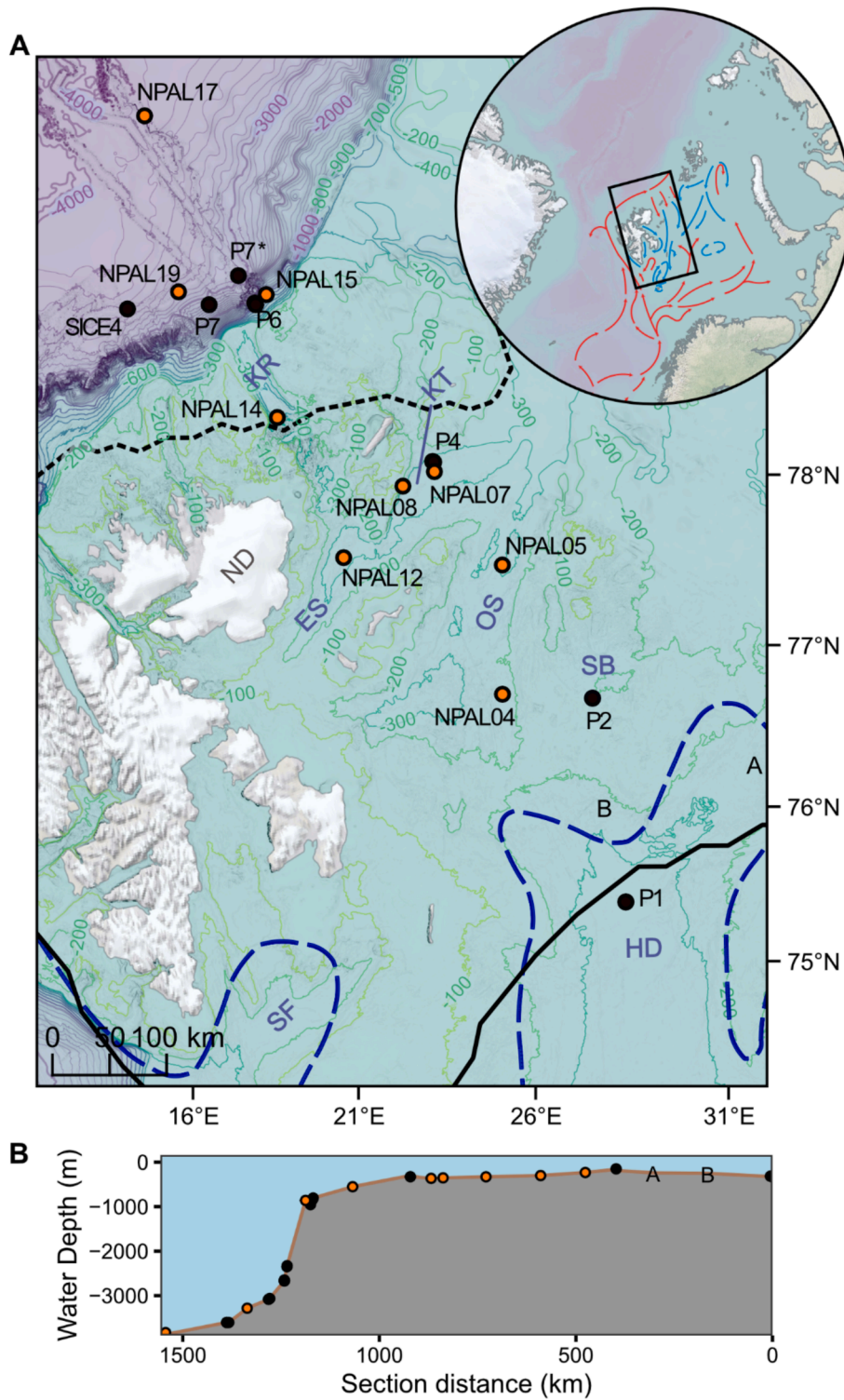
Fig. 1. (A) Bathymetric map of the study area in the northern Barents Sea, including the sample locations. (B) Water depth transect and section distance. Orange circles indicate the location of dated sediment cores and black circles indicate sites sampled in the seasonal studies. Project EISA sampling sites are stations A (250 m) and B (241 m). More information on the location of the studied cores is available in the Supplement Material (Table S1). Summer and winter median sea ice extent (1981–2010, NSIDC − Fetterer et al., 2017) are shown as black dashed and solid lines, respectively. The blue dashed line indicates the polar front location. Red arrows indicate the relatively warm Atlantic Water and the light blue arrows represent the colder Polar Water (Loeng, 1991; Lundesgaard et al., 2022). ND = Nordaustlandet, ES = Erik Eriksenstretet, KR = Kvitøyrenna, KT = Kong Karls Trough, OS = Olgastretet, SB = Storbanken, HD = Hopendypet and SF = Storfjordrenna. Database: IBCAO version 4.0 (Jakobsson et al., 2020).

sea ice concentration, water depth, distance to land, and chlorophyll-a concentration. Temperature, salinity, and oxygen values were retrieved from compiled data from CTD casts deployed on each Nansen Legacy cruise (Gerland, 2022; Husum, 2022; Ludvigsen, 2022; Reigstad, 2022; Søreide, 2022). Data from CTD casts of SSQ3 closest to stations A and B were used as the cruises occurred in the same period. The chlorophyll concentration (Chla) data for all stations was obtained from previously published measurements from CTD casts with Niskin bottles (Nöthig et al., 2018 – proximal to stations NPAL04, NPAL12 and NPAL14; Vader, 2022). For the sea ice concentration, we used monthly mean ice concentrations of 1978–2021 from the Sea Ice Index version 3 provided by the National Snow and Ice Data Centre (NSIDC – Fetterer et al., 2017). The monthly concentrations are provided in a georeferenced format from Nimbus-7 SMMR and DMSP SSM/I-SSMIS Passive Microwave Data (DiGirolamo et al., 2023). Based on the sampling coordinates, we calculated the seasonal averages from the monthly ice concentrations values defined as follows: Winter: January, February, and March; Spring: April, May, and June; Summer: July, August, and September; Fall: October, November, and December. The distance to land was based on NASA's Ocean Biology Processing Group – 0.1x0.1 degree – Distance to the Nearest Coast (Stumpf, 2009).

2.3. Age determination

Sub-samples from all NPAL sediment cores were analysed for ^{210}Pb, ^{226}Ra, and ^{137}Cs activities by direct gamma assay in the Liverpool University Environmental Radioactivity Laboratory using well-type germanium detectors (Appleby et al., 1986). Supported ^{210}Pb activity (^{210}Pb$_{sup}$) was assumed equal to the measured ^{226}Ra activity in the sediments. Unsupported ^{210}Pb activity (^{210}Pb$_{unsup}$) was calculated by subtracting ^{210}Pb$_{sup}$ from the measured total ^{210}Pb activity (^{210}Pb$_{total}$). Raw ^{210}Pb dates were calculated from ^{210}Pb$_{unsup}$ profiles using both the constant rate of supply (CRS) and constant initial concentration (CIC) models (Appleby and Oldfield, 1978), and also mixing models where thought applicable (Oldfield and Appleby, 1984). Where possible, chronostratigraphic dates were determined from ^{137}Cs profiles recording specific fallout events. The sediment cores chronologies were based on an assessment of all data (^{210}Pb, ^{137}Cs) using the methods outlined in Appleby (2001). Sedimentation rates were calculated in terms of both volume (sediment thickness per unit time, SR – cm y^{-1}), and dry matter (dry mass increment per unit area and time – sediment accumulation rates, SAR – g m^{-2} y^{-1}).

2.4. Geochemical and grain size analyses

A subsample (~1 g) of freeze-dried sediment from each core slice was homogenised and pulverised prior to total organic carbon (TOC), total carbon (TC), total nitrogen (TN) and carbon (δ^{13}C) and nitrogen stable isotope (δ^{15}N) analyses. These sediment parameters were analysed for the core top 6 cm of seasonal stations, site A (site B: 4 cm), and the top 10 cm of NPAL- stations. Elemental analysis of carbon and nitrogen concentrations was undertaken with an Elemental Analyser – Isotope Ratio Mass Spectrometry (EA-IRMS; Iso-Analytical Ltd., UK). While total carbon and total nitrogen were analysed in non-acidified bulk sediments, prior to TOC and δ^{13}C analyses, it was necessary to remove inorganic carbon. Samples were acidified with 1 M HCl and left overnight to allow the inorganic carbon to be liberated as CO$_2$. The samples were neutralized by repetitively washing with distilled water and subsequently oven drying at 60 °C. The measured TOC content was corrected for weight loss upon acid washing. Measured isotope ratios (R$_{sample}$) were compared with known ratios of external references (R$_{standard}$), expressed as

$$\delta(‰) = \left(\frac{R_{sample} - R_{standard}}{R_{standard}} \right) * 10^3$$

The reference standards IA-R001, IA-R005 and IA-R006 (wheat flour, beet sugar, cane sugar) were used to calibrate δ^{13}C values against IAEA-CH-6 (international standard sucrose). For δ^{15}N calibration, wheat flour and ammonium sulphate (IA-R001, IA-R045 and IA-R046) were used against IAEA-N-1 (international standard ammonium sulphate). The δ^{13}C and δ^{15}N analysis proceeded in a batch process by which a reference is analysed followed by a number of samples and then another reference. The isotope ratios analytical error was determined by calculating the standard deviation of repeated measurements of reference standards (≤ 0.07 ‰ for δ^{13}C and ≤ 0.15 ‰ for δ^{15}N). Total inorganic carbon (TIC) was calculated by subtracting TOC from TC. TIC will be considered a proxy for CaCO$_3$ content since it is often estimated as a product between TIC and CaCO$_3$ density. The organic carbon accumulation rate (AR$_{toc}$, g m^{-2} y^{-1}) was calculated by multiplying SAR and TOC content (g/g) in each sample.

Grain size distribution of non-acidified samples was assessed with a Beckman Coulter LS 13 320 Particle Size Analyser. The organic matter was removed with 10 % H$_2$O$_2$ and deflocculated with a 5 % Calgon solution (sodium hexametaphosphate and sodium carbonate) in an ultrasonic bath prior to analysis. The particle diameter within the 0.04–2000 μm range was measured at 0.004 μm resolution. The TOC content was adjusted to the sediment fine fraction (<63 μm – according to Norwegian guidelines; Veileder, 2018) by using the following equation: ($TOC_{63} = TOC + 18 \times (1 - <63\mu m)$). The grain size data were used as an environmental explanatory variable in the statistical analyses.

2.5. Statistical methods

The following spatial data analysis was confined to the top (0 to 6 cm) individual sediment layers to allow comparisons between stations. All statistical analyses were performed in R (R Core Team, 2020). A generalised additive model (GAM) was conducted with the R package mgcv (Wood, 2017) to explore the relationship between a smoothed function of latitude and water depth and the geochemical parameters (e. g., TOC$_{63}$, TIC, TN). To identify spatial differences in geochemical data distribution, the spatial data (latitude and longitude) were converted to UTM and used to compute distance-based Moran's eigenvector maps (dbMEM, Dray et al., 2021). The eigenvectors that showed significant explanatory power (MEM axes 1–10) were used as predictors of the effects of spatial scales. We also forward-selected the environmental variables (e.g., water depth, grain size, SST) using the undetrended geochemical data (Borcard et al., 2018). This was followed by redundancy analysis (RDA) and variation partitioning (VP) analysis with the selected spatial and environmental explanatory parameters; both were performed using the *vegan* package. The RDA analysis allowed us to evaluate and test the relationship of multivariate response data (geochemical variables) with multiple (potential) explanatory factors (environmental parameters and spatial structure) (Dray et al., 2012; Borcard et al., 2018). The significance of the constrained RDA model was tested by a permutation test with 1,000 permutations; highly correlated variables (p < 0.01) were removed from the model to avoid collinearity. The VP analysis quantifies the fraction of geochemical data variation explained solely by the spatial attribute, environmental parameters, or spatially structured environmental variation (Borcard et al., 1992).

3. Results

3.1. Sediment chronology

Core depths at which total ^{210}Pb activity reached equilibrium with the supporting ^{226}Ra varied from no more than a few centimetres at the Arctic basin station (NPAL19), to as much as 16 cm at NPAL08 in the Kong Karls Trough (Fig. 2). Two sites, NPAL04 and NPAL17, had nearly constant ^{210}Pb concentrations throughout a substantial part of the
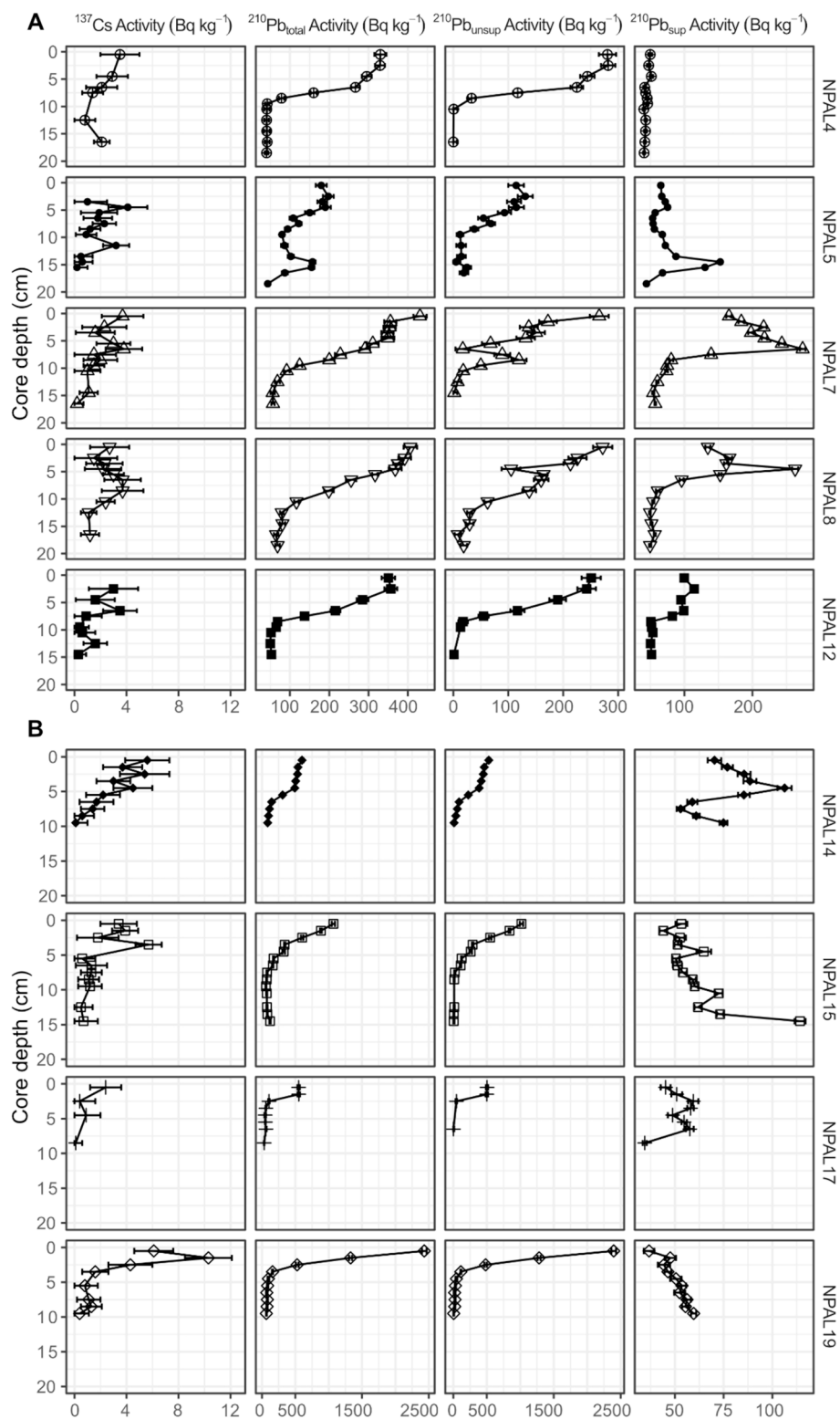
Fig. 2. Vertical distribution of ^{137}Cs and ^{210}Pb activities in the sediment cores from the northern Barents Sea (NPAL sites). (**A**) Southern, shallower shelf sites. (**B**) Northern, deeper slope and Arctic Basin sites. The horizontal bars indicate standard error. A summary of the radionuclide concentrations can be found in the Supplementary Table S3.

record. Since this could indicate intensive sediment mixing, these cores were not considered to have reliable chronological records. ^{226}Ra (i.e. ^{210}Pb$_{sup}$, Fig. 2) concentrations were typically in the range 44–65 Bq kg^{-1}, though several sites, principally those located east of Nordaustlandet, contained layers of sediment with much higher concentrations.

At two of those sites (NPAL07, NPAL08, Fig. 2), peak ^{226}Ra concentrations reached values in excess of 250 Bq kg^{-1}.

Unsupported ^{210}Pb concentrations had their highest values at or close to the sediment–water interface (Fig. 2). Table S2 summarizes a number of key radiometric parameters for each core, including the

^{210}Pb$_{unsup}$ surficial concentration, inventory and flux (mean supply rate), the 90 % ^{210}Pb/^{226}Ra equilibrium depth, and the ^{137}Cs inventory. The 90 % equilibrium depth corresponds to around 75 years accumulation. The results show that the surficial ^{210}Pb concentrations and mean ^{210}Pb fluxes are significantly related to (A) the water depth and (B) the 90 % equilibrium depths (or equivalently, the mean sedimentation rates; Figure S3). At sites on the northern Barents Sea shelf up to a water depth of 1000 m, values of both parameters increase more or less linearly with water depth, surficial ^{210}Pb concentrations from 114 Bq kg^{-1} at NPAL05 to 1017 Bq kg^{-1} at NPAL15, and fluxes from 133 Bq m^{-2} y^{-1} to 461 Bq m^{-2} y^{-1}. There are further but relatively smaller increases towards the abyssal site (NPAL19, water depth 3283 m) where the surficial ^{210}Pb concentration was 2396 Bq kg^{-1} and the flux 496 Bq m^{-2} y^{-1}. Concentrations and inventories of ^{137}Cs were generally very low but showed reasonably well-defined concentration peaks in several stations (NPAL19, NPAL15, NPAL08; Fig. 2). In the shelf cores, maximum ^{137}Cs concentrations ranged between 3.5 and 4 Bq kg^{-1}, though slightly higher values were recorded in sites near the shelf boundary. A

significantly higher value was recorded at NPAL19 (10.3 Bq kg^{-1}, Fig. 2).

Sediment chronology and accumulation rate for NPAL19 in the Arctic basin were relatively unequivocal. Unsupported ^{210}Pb concentrations declined almost exponentially with core depth and the CRS and CIC models both suggested a low but relatively constant sedimentation rate, with a mean SAR of 130 g m^{-2} y^{-1} (0.031 cm y^{-1}; Fig. 3B). The corresponding ^{210}Pb dates suggested that the ^{137}Cs concentration peak in the 1–2 cm layer is a record of fallout from the 1986 Chernobyl accident (Fig. 3A). At the shelf sites, and most particularly at NPAL05, NPAL07, NPAL08, and NPAL12, the ^{210}Pb$_{unsup}$ records diverged significantly from a simple exponential decline indicating non-uniform sedimentation. Dates for these sites were calculated using the CRS ^{210}Pb dating model. At stations where the ^{137}Cs record contained a feature identified as originating in fallout from the 1986 Chernobyl accident (NPAL08, NPAL15), the CRS model dates were consistent with the ^{137}Cs date (Fig. 3A). Standard uncertainties in the CRS model dates typically increased from 1 or 2 years near the top of the core to around 8 years at
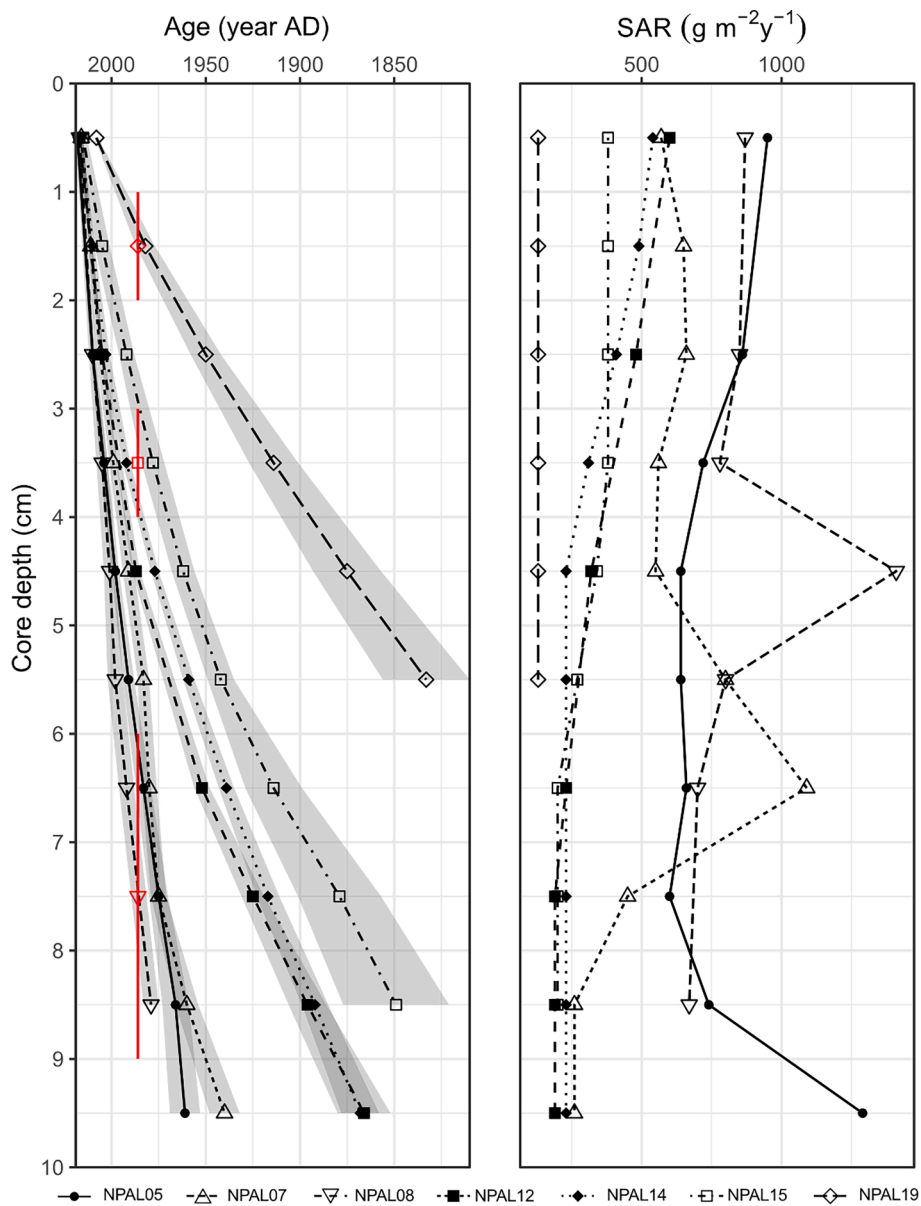

Fig. 3. (**A**) Age–depth model based on ^{210}Pb chronology of the NPAL- cores; the shaded gray areas indicate standard deviation. Peaks in the ^{137}Cs records attributed to fallout from the 1986 Chernobyl accident were identified in three cores (NPAL08, NPAL15, NPAL19), their depths and uncertainties are marked by red symbols and bars. (**B**) Sediment mass accumulation rate (SAR) for the different stations.

the 90 % equilibrium depth (75 years), with proportional increases at greater depths.

Mass sediment accumulation rates (SAR) for sites NPAL12, NPAL14, and NPAL15 were low and relatively uniform in the early 20th century but subject to a steady acceleration since then (Fig. 3B). The increases at NPAL15 occurred mainly during the middle decades of the 20th century, whereas at NPAL12 and NPAL14 were more recent and pronounced. Records at the other shelf sites are much more irregular. Sedimentation rates at NPAL08 are substantially higher than at NPAL07 but follow a similar pattern. At both sites, an earlier period of relatively uniform accumulation is punctuated by a brief episode of rapid accumulation. This event is dated to the early 1980 s at NPAL07, and the late 1990 s at NPAL08. At NPAL07 it is recorded by a major non-monotonic feature in the ^{210}Pb record between 5 and 8 cm. The impact at NPAL08 is confined to the 4–5 cm layer. Both events appear to be broadly related to a substantial increase in ^{226}Ra concentrations, presumably due to change in sediment source. The ^{226}Ra concentrations at NPAL07 increased from 81 Bq kg-1 in the 8–9 cm to a peak value of 274 Bq kg-1 in the 6–7 cm layer. At NPAL08 they increased from 62 Bq kg-1 in the 10–11 cm to 263 Bq kg-1 in the 4–5 cm layer. Calculations for NPAL05 suggest a similar sedimentation rate to that at NPAL08, though with an earlier episode of rapid sedimentation. Because of the high ^{226}Ra

concentrations in sediments below 9 cm (Fig. 2, unsupported ^{210}Pb concentrations in this part of the record barely exceed detection limits), SAR values and chronologies of sediments in NPAL05 below this depth (pre-1960 s) have large uncertainties.

3.2. Spatial trends in geochemistry

Most geochemical parameters show a clear contrast between the deeper Arctic Basin and the shelf stations (Fig. 4). The TOC_{63} content ranged from 0.6 % to 2.6 %; higher average values of 2.40 ± 0.11 % and 2.35 ± 0.04 % were found at the southern stations P1 and NPAL04, respectively, whereas the deep Arctic basin stations NPAL17 and SICE4 had low TOC_{63} average values: 0.77 ± 0.10 % and 0.98 ± 0.17 %, respectively. A latitudinal trend in TOC_{63} (Fig. 4, Table S4), not closely related with water depth, indicates the variability of organic carbon within the Barents Sea shelf. The analysis shows a clearer trend between TN and water depth (Fig. 4, Table S4), as well as with latitude. Southern and shallower stations have higher TN values than northern and deeper stations (TN ranged from 0.07 % to 0.33 %). TIC content showed the opposite trend with latitude and water depth, with higher average values (1.28 ± 0.02 % at NPAL19) in the Arctic Basin and lower in the southern Barents Sea shelf (0.25 ± 0.09 % at P1). The C_{org}/N_{total} ratio
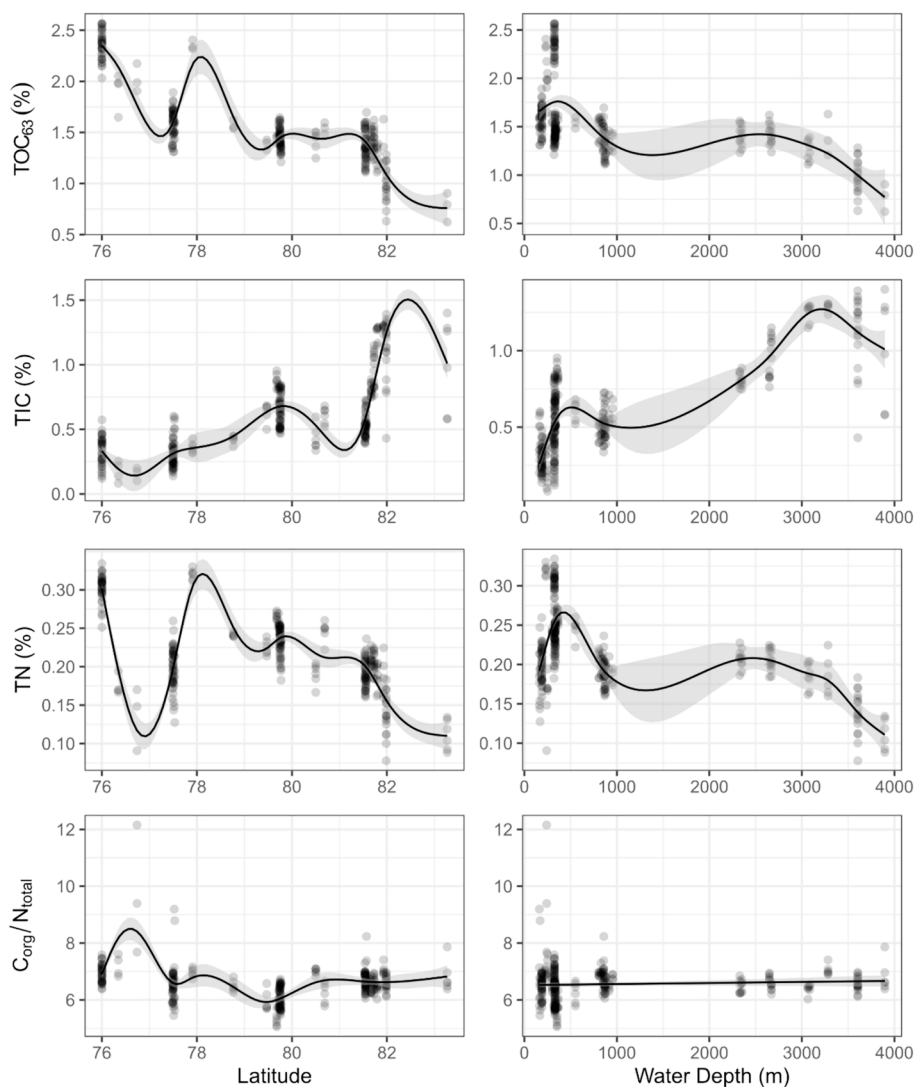

Fig. 4. General additive model (GAM) indicating the distribution of TOC_{63}, TIC, TN, and C_{org}/N_{total} values in relation to latitude and water depth. Each dot represents an individual measure, the black line represents the fitted curve of each independent variable, the gray area represents the 95 % confidence interval. A summary of the GAM results can be found in the Supplementary Material (Table S4).

was at or below Redfield (5.65–7.86), and there was no evidence of a relationship between C_{org}/N_{total} ratio and water depth or latitude (Fig. 4, Table S4). Stations B (9.74 ± 2.25) and A (7.19 ± 0.37) in the southern Barents Sea had higher ratios, driven by low TN values around 3 cm sediment depth. Considering the illite enrichment in sediments in the northern Barents Sea (Vogt and Knies, 2009) and its effect on total nitrogen content (Winkelmann and Knies, 2005), the TN and C_{org}/N_{total} results will not be considered to assess sources of organic matter in this study.

3.3. Seasonal and vertical trends in sediment geochemistry

Due to a one-year gap between seasonal cruises in 2019 and 2021, sampling of a full seasonal cycle was not possible. Thus, seasonal changes include a one-year variation between fall and winter. In general, there were no differences in the geochemical parameters among the distinct seasonal campaigns. One exception is at P7, where the TIC content was highest during spring (1.3 % − SSQ2) and lowest during summer (0.9 % − SSQ3). At P2 during winter (SSQ1), the C_{org}/N_{total} ratio decrease down-core and coincided with the lowest $\delta^{13}C$ (−24.1 ± 0.2 ‰) during the same period.

The down-core profiles represent long-term changes due to time-averaging. Most down-core profiles of measured parameters indicated little variability. At the northernmost stations (SICE4 − Fig. 5; NPAL15 and NPAL19 − Fig. 6), however, the surface TOC_{63} was 1.3–1.6 % and decreased with core depth to 0.6–1.2 %. Sediment depth profiles of TN remained constant for most stations except P2 during winter. The sediment TIC content also had higher values at the surface (0.6–1.4 %) and decreased (0.2–0.4 %) down-core at stations NPAL08, NPAL12 and SICE4. Stratigraphically, the C_{org}/N_{total}, $\delta^{15}N$ and $\delta^{13}C$ did not display considerable down-core changes (Fig. 6). The TOC accumulation-rate (AR_{toc}) profiles showed higher values at the sediment surface (Fig. 6). An increasing trend in AR_{toc} appeared to have initiated around the 1970s. The down-core peaks in AR_{toc} at stations NPAL05, NPAL07 and NPAL08 might be linked to rapid sedimentation events that are reflected by higher SAR (Fig. 3).

3.4. Grain size

The grain size distribution showed the predominance of silt–clay fractions in all studied sites (Figs. 5, 6). Stratigraphically, stations presented mean grain size fluctuations, while clay, silt, and sand frequency were generally uniform. Mean grain size showed a slight increase in recent years (1970s onwards). Surface sand content was highest in the sediments of the southern Barents Sea shelf (P1, P2, stations A and B), ranging between 12 and 33 % and mean grain sizes being >23 μm. While TOC_{63} is highly correlated with TOC and follows the same spatiotemporal trends, stations with higher sand content (A, B, P1 and P2) showed an elevated degree of TOC dilution due to differences in particle size (Fig. 7A).

3.5. Environmental drivers of sediment geochemistry

The distance-based Moran's eigenvector maps (dbMEM) and forward selection analysis resulted in five significant eigenfunctions showing a positive spatial autocorrelation. Each eigenvector selected represents the range of broader spatial structures (MEM1, MEM2, MEM3, 1000kms to 100kms) to medium and fine scales (regional to local structures − MEM4, MEM5, 100kms to 10kms) (Borcard et al., 2018). The forward selection analysis in the environmental component selected seven variables that significantly explained the geochemical parameter distribution: winter sea ice concentration, summer sea ice concentration, sand content, chlorophyll-*a* concentration, water depth, clay content, sea bottom temperature (SBT), sea bottom salinity (SBS) and silt content. The plots from the *vegan* package function *ordisurf* delineate the dbMEM and the environmental drivers ordination in relation to the geographical

coordinates (Figure S2). The RDA analysis (Fig. 8) explained 84 % of the variability in sedimentary geochemical components, with the first two axis accounting for 66 % of the constrained variation. The first axis summarized the variability at a broader scale (MEM3) associated with the gradient from the region covered by sea ice during winter, north of the Polar Front, with lower productivity and high $\delta^{15}N$ concentrations to southern stations with higher primary production (i.e. chlorophyll-*a*, TOC_{63} and enriched $\delta^{13}C$), higher bottom temperatures, and sandy sediments. The second axis spatially separated sites with high sand content, high C_{org}/N_{total} ratio and chlorophyll-*a* from the deeper stations with high silt, clay and TIC content. In this axis, the MEM2 vector describing broader spatial structures, was highly correlated with silt and TIC distribution (Fig. 8), which were lower at southern stations at banks and around the Polar Front (Figure S2). The variance partitioning analysis indicated that environmental variables explained around 72 % of the sedimentary geochemical data variation, of which 22 % was not spatially structured. About 50 % was related to broad scale environmental variations and 4 % to regional environmental variations. The variation explained by spatial variables independent of the environment was low (5 % − broad scale, 2 % − fine scale MEM variables).

4. Discussion

4.1. Radionuclide spatial variability

The processes by which unsupported ^{210}Pb reaches the seabed are highly complex, and not amenable to deterministic modelling in any realistic way. In lake sediments the $^{210}Pb_{unsup}$ source is almost entirely atmospheric fallout either directly onto the surface of the lake, or indirectly via the catchment. In the marine environment, however, even though factors such as winter ice cover and sediment focusing may play a role, a significant fraction likely derives from ^{226}Ra decay in the water column. Unsupported ^{210}Pb inventories in eight lake sediment cores from nearby Svalbard (1455–7904 Bq m^{-2}, with a mean value of 3204 Bq m^{-2}; Appleby, 2004) were significantly lower than the mean inventory (5846 Bq m^{-2}) for the four adjacent shelf sites (NPAL05 − NPAL12). Higher inventories and elevated ^{210}Pb concentrations in cores near the shelf edge and beyond in the Arctic Basin can be attributed to the longer water residence times and thus increased levels of ^{210}Pb enrichment at these sites (Table S2, Fig. 2B). Despite these complexities, the credibility of the results presented here and of the CRS model used to calculate the sediment dates suggests that the supply of $^{210}Pb_{unsup}$ at the study sites has been relatively constant when averaged over the few years typical of each core slice.

4.2. Sediment accumulation rates and ^{210}Pb chronologies

Overall, the average sediment accumulation rates (SAR) (and volumetric sedimentation rates, SR) from the sampled stations ranged between 130 and 823 g m^{-2} y^{-1} (0.03–0.18 cm yr^{-1}, Table 1). Although there is a high variability in average SAR at the shelf stations, there is a decreasing trend towards the slope and basin sites ($R^2 = 0.75$, p < 0.001), which was not observed in previous studies (Carroll et al., 2008a; Zaborska et al., 2008; Maiti et al., 2010). The SR values in Svalbard fjords (0.1–0.6 cm yr^{-1}; Kim et al., 2020) and the eastern Barents Sea near river mouths (~0.1–0.2 cm yr^{-1}; Smith et al., 1995) were generally higher than those observed for the northern Barents Sea in this study. Other SARs recorded in the northern Barents Sea shelf were similar to this study for comparable water depths as they were often sampled at shallower sites or closer to the Svalbard coast (e.g., Carroll et al., 2008a; Zaborska et al., 2008; Maiti et al., 2010).

While bioturbation has been identified as a relevant mixing process in Barents Sea sediments (Maiti et al., 2010; Oleszczuk et al., 2019), there is a high spatial and temporal variability in the region associated with changes in benthic communities, food supply, and other environmental factors (Oleszczuk et al., 2019; Solan et al., 2020). Moreover,
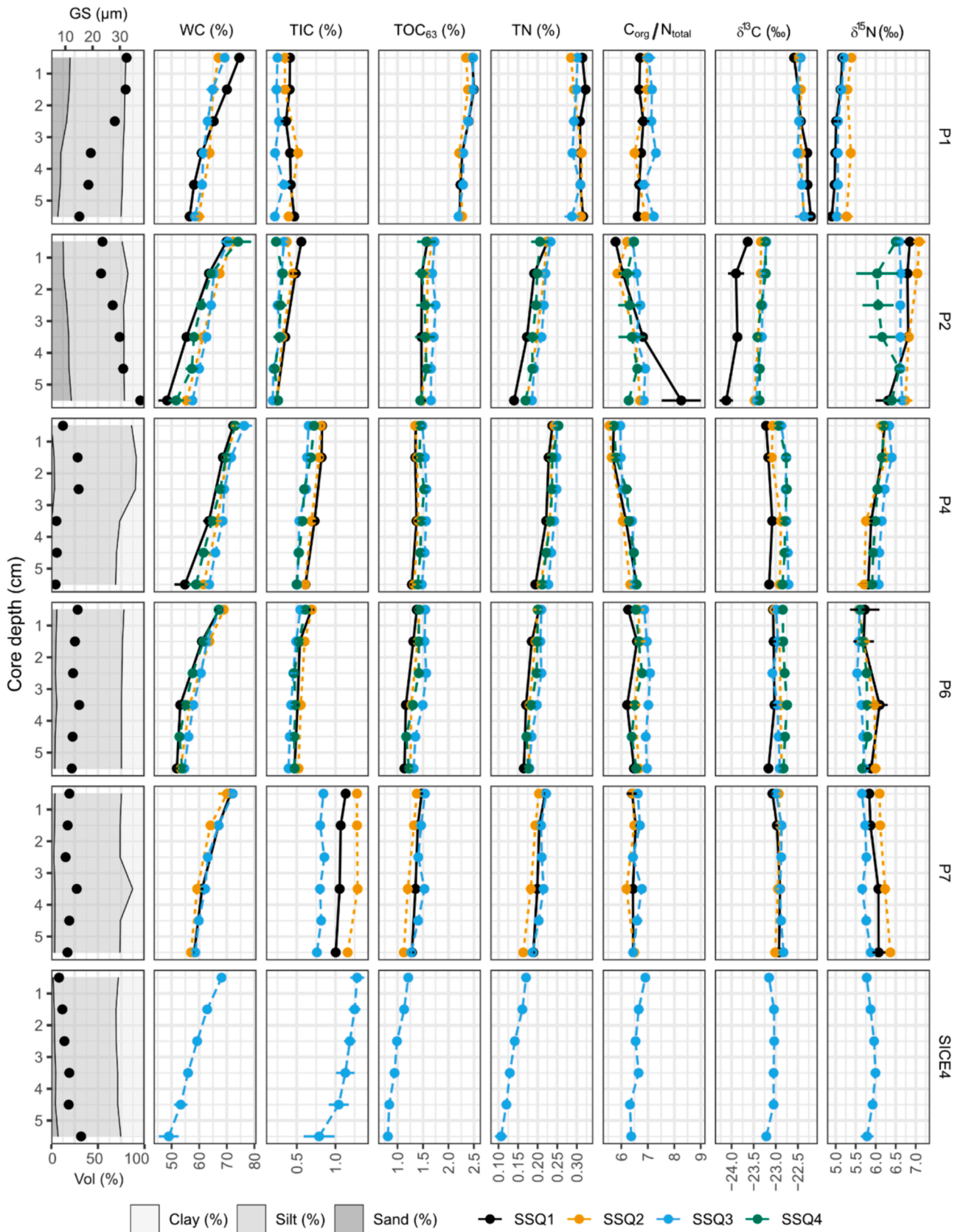
Fig. 5. Vertical profiles of mean grain size (GS, left black dots), cumulative volume of grain size fractions (Vol %), water content (WC), TIC, TOC_{63}, TN, C_{org}/N_{total}, $\delta^{13}C$ and $\delta^{15}N$ average ± standard error of cores collected during the seasonal campaigns (SSQ1 to SSQ4). The colors represent the different seasonal campaigns.
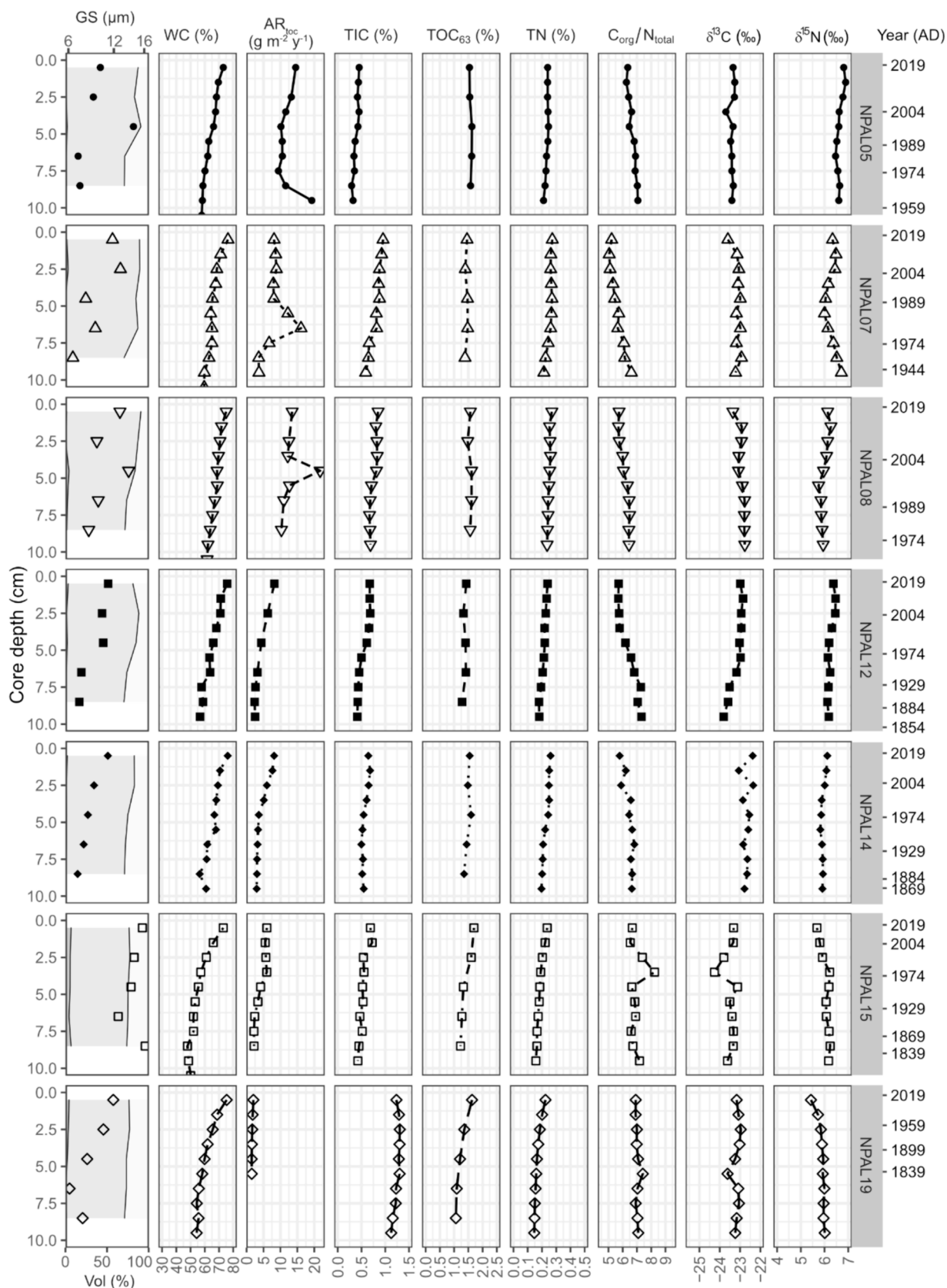
Fig. 6. Vertical profiles of mean grain size (GS, left symbols), cumulative volume of grain size fractions (Vol %), water content (WC), AR_{toc}, TIC, TOC_{63}, TN, C_{org}/N_{total}, $\delta^{13}C$ and $\delta^{15}N$ of the NPAL- cores with estimated ages (Year AD). The symbols represent the different stations.
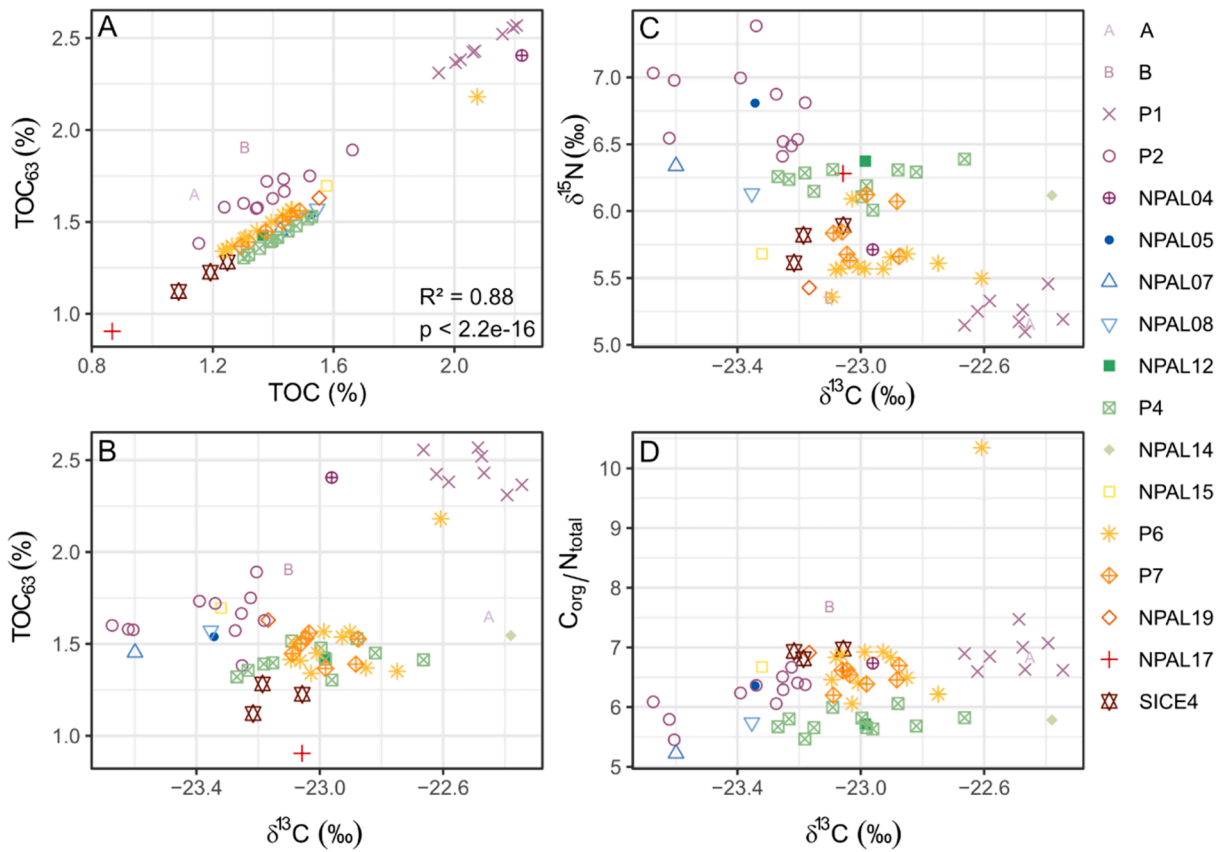
Fig. 7. (**A**) Relationship between TOC and TOC_{63}, (**B**) TOC and $\delta^{13}C$, (**C**) $\delta^{15}N$ and $\delta^{13}C$, and (**D**) C_{org}/N_{total} ratio and $\delta^{13}C$ in the sampled sediments. Colors and symbols represent the different stations.
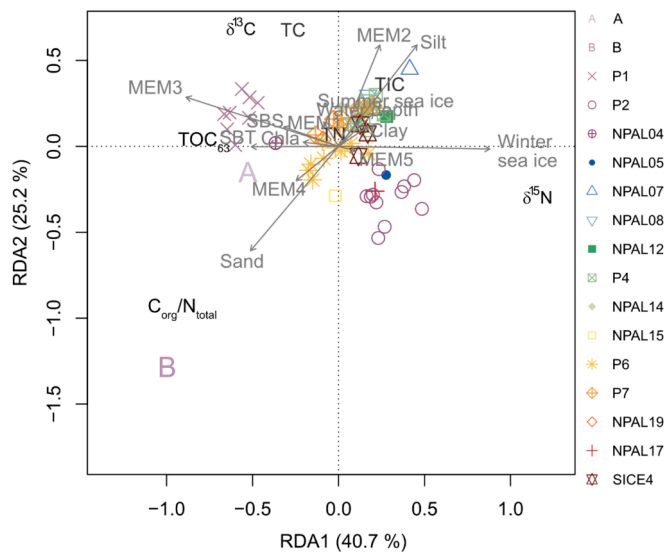
Fig. 8. Redundancy analysis (RDA) biplot of the geochemical parameters and sample sites in relation to the environmental predictors and the main spatial gradients (eigenfunctions from dbMEM). Colors and symbols represent the different stations. Abbreviations: SBT = sea bottom temperature, SBS = sea bottom salinity, Chla = chlorophyll *a* (Vader, 2022), MEM = Moran's eigenvector maps. Detailed correspondence table used in the analysis is available in the Supplementary Datasheet S1.

only minor sediment stratigraphy disturbances were observed in previous studies (Carroll et al., 2008b; Faust et al., 2021). Thus, in the dated sediment profiles of this study, the absence of zones of near constant

^{210}Pb activity in the surficial sediments and preservation of ^{226}Ra-rich layers with well-resolved concentrations peaks suggests no substantial effects of sediment mixing on the estimated SAR and SR.

The ^{210}Pb records from the Barents Sea cores show a consistent pattern, apart from two sites where the records appeared either incomplete (NPAL17) or disturbed (NPAL04, Fig. 2, Table 1). The near exponential activity versus depth relation at NPAL19 indicates a stable regime at that site. Sites NPAL05 – NPAL08 appear to have experienced more significant changes, affecting both the supported and unsupported ^{210}Pb records. The presence of ^{226}Ra-rich layers suggests significant shifts in sediment source in the recent past. These sites are located in deeper parts of Olgastretet (NPAL05) and of Kong Karls Trough (KT, NPAL07 and NPAL08), with pronounced moraines and wedges (Husum et al., 2020). The peaks (around the 1990s, 1980s and 2000s, respectively) and increase in SAR are associated with an up-core increase in silt and mean grain size (Fig. 6). While lag deposits can be found on the shallow platforms surrounding Kvitøya and Kong Karls Land (Elverhøi et al., 1989), moderate bottom current velocities were recorded for a shallower portion of OS (10–31 cm s^{-1}), with enough velocity for sediment resuspension during winter and fall periods (Sternberg et al., 2001). These sediment profiles are distinct from the profile from Erik Eriksenstretet (ET, NPAL12), where concentrations of ^{226}Ra rich sediments are relatively uniform and have a lower mean value (102 Bq kg^{-1}), while the mean grain size and SAR also increase after the 1960 s but does not show a peak. This suggests that deposition events at KT and NE Olgastretet are the result of a possible near erosion event that focused sediment deposition in these depressions areas of the shelf, in contrast to the ET region, where the enhanced sedimentation and steady ^{210}Pb profiles indicate a continuous deposition process (Paradis et al., 2017). A corresponding age model was observed for two cores based on AMS ^{14}C dates from NPAL08 (5.5 cm, 1957–2007 cal. yr AD) and NPAL14 (5.5

Table 1

NPAL sediment cores locality, water depth, dated core length, age range, sediment mass accumulation rate (SAR) and organic carbon accumulation rate (AR$_{toc}$). AR$_{toc}$ range refers to the core top 10 cm where TOC was measured.

Station	Region	Water depth	Core length	Age range	SAR	AR$_{toc}$
		(m)	(cm)	(AD)	(g m^{-2} y^{-1})	(g m^{-2} y^{-1})
NPAL04	Southern Olgastretet	232			Sediment mixing	
NPAL05	Northern Olgastretet	301	16.5	1919–2019	0.060–0.129	9.41–14.50
NPAL07	Kong Karls Trough	353	12.5	1878–2019	0.026–0.109	3.59–16.06
NPAL08	Kong Karls Trough	364	18.5	1901–2019	0.067–0.141	10.28–21.70
NPAL12	Erik Eriksenstretet	329	9.5	1866–2019	0.019–0.060	2.39–8.19
NPAL14	Kvitøyrenna	552	9.5	1868–2019	0.023–0.054	3.00–8.12
NPAL15	Upper Kvitøyrenna Mouth Fan	859	8.5	1849–2019	0.020–0.038	2.18–5.99
NPAL17	Arctic abyssal plain	3,896			Sediment mixing	
NPAL19	Arctic abyssal plain	3,283	5.5	1833–2019	0.013	1.51–2.01

cm, 1675–1957 cal. yr AD), and support the reliability of the presented age model (Pieńkowski 2023, pers. comm.).

4.3. Spatial and environmental drivers of sediment geochemistry

While the temporal variability in organic carbon content was low, there is high spatial variability in TOC$_{63}$ distribution in the northern Barents Sea. The TOC$_{63}$ values observed in this study are consistent with previous reports pointing at high concentrations at shelf sites and low values at Arctic Basin sediments (Zaborska et al., 2008; Knies and Martinez, 2009; Faust et al., 2020). Other sedimentary parameters, such as TN and δ^{13}C, were also consistent with observations from other studies (e.g., Knies and Martinez, 2009). Still, the non-linear relationship of most sedimentary parameters with latitude and water depth (Fig. 4) has also been described by others (Winkelmann and Knies, 2005; Carroll et al., 2008a; Knies and Martinez, 2009; Faust et al., 2020). This indicates that distinct and characteristic geomorphological features, productivity patterns and sea ice regimes for the Barents Sea and Arctic basin are the main drivers of the distribution of the geochemical parameters (e.g., TOC$_{63}$).

4.3.1. From the shelf to the slope

The multivariate analysis enabled us to access the spatial scales that contributed most to the variation in response data (e.g., organic carbon content) and to what extent they correlated with the spatial variation in the environmental variables (e.g., water depth). We found that spatial and environmental drivers separately explain a low amount of variation in the geochemical parameters, whereas spatially structured environmental drivers are the main contributors to the variation. In addition, large-scale spatial gradients are more important to explain geochemical properties than small-scale variability. It's important to note that smaller scale variability can still occur in the region, even though they were not as significant in this studied transect. The TOC$_{63}$ and δ^{13}C were negatively associated with winter sea ice concentration and positively associated with SBT, SBS, and Chl*a* (Fig. 8), i.e., areas with low sea ice coverage (Figure S1) and more influenced by Atlantic waters (Jones et al., 2023) have high primary production and possibly more organic carbon reaching the sea bottom (Bodur et al., 2023). This suggests that the variation in sea ice concentration linked with AW inflow that affects phytoplankton growth (Falk-Petersen et al., 2000) and export production (Anglada-Ortiz et al., 2023), regulate sediment biogeochemistry in the study area.

Southern stations in the studied transect have the highest organic carbon content, however, they are less similar in TOC$_{63}$ compared to northern sites. The general broad scale pattern is associated with the effect of high biological production, sea-bottom temperature and salinity (Chl*a*, SBT and SBS, Fig. 8), more variable grain size distribution, and is inversely related to winter sea ice concentration on the southern sites (Fig. 8). This is supported by the radionuclide's spatial

variability. The shelf stations under seasonal sea ice cover in our study have generally low ^{210}Pb$_{unsup}$ activities, yet higher surface values are found at southern Olgastretet (NPAL04) when compared to other shelf stations (Fig. 2, Tables S2, S3). In this region, there are previous records of high biogenic flux to the bottom (Wexels Riser et al., 2008), which can enhance ^{210}Pb scavenging in the water column (Cochran et al., 1990). A high ^{210}Pb$_{unsup}$ activity in deeper shelf areas associated with high productivity was also observed by Zaborska et al. (2008), who recorded high ^{210}Pb$_{unsup}$ activity values (350–720 Bq kg^{-1}) associated with high TOC content (2.0–2.5 %) at Hopendypet (HD), south of the Polar Front (PF). On the other hand, shallower sites near the PF had lower TOC$_{63}$ content and δ^{13}C (Fig. 7B). These low organic carbon values were reported by Knies and Martinez (2009) and could be associated with higher bottom current speed in bank areas (Elverhøi et al., 1989) that winnow away fine sediments and associated OC. Shallower stations near the Spitsbergen coast, that are associated with higher bottom current velocity (Sternberg et al., 2001) also had lower ^{210}Pb$_{unsup}$ activity and TOC content (Zaborska et al., 2008; Carroll et al., 2008a; Maiti et al., 2010). Other studies in this region registered a high contribution of faecal pellets with low δ^{13}C to the total POC vertical flux (Tamelander et al., 2008; Wexels Riser et al., 2008). Fecal pellets sink faster with little degradation to the seafloor and explain lower δ^{13}C values when compared with enriched southern stations (Fig. 7B). Moreover, a low chlorophyll *a* flux and a depleted δ^{13}C signal of sinking OM in the shallowest shelf stations were recorded from sediment traps along the same transect (Bodur et al., 2023). This suggests that while sea ice concentration and primary production gradients influence the south and north of the Polar Front sediment geochemistry patterns, regional factors such as nutrient-depleted polar surface water relative to AW (Erga et al., 2014; Bodur et al., 2023), granulometry and water depth associated with water mass characteristics might also affect heterogeneity in geochemical properties.

4.3.2. Signal of Atlantic water intrusion

Besides the high ^{210}Pb$_{unsup}$ surface activities found at southern Olgastretet (OS) station (NPAL04), the TOC$_{63}$ content observed is similar to the organic carbon content of the Hopendypet station (P1), while it contrasts with the nearest stations also located north of the Polar Front (P2 and NPAL05, Fig. 7). The saddle between Olgastretet and Hopendypet allows AW to cross the Polar Front, especially during winter periods when AW is pushed upslope (Lind and Ingvaldsen, 2012; Lien and Trofimov, 2013). This part of the AW that crosses the Polar Front may explain the high SBT, SBS and chlorophyll-*a* associated with this station (Fig. 8), as the more saline water near the bottom of Olgastretet is evident (Lind and Ingvaldsen, 2012). The intrusion of AW can potentially increase sea ice melt and influence biological production in the Barents Sea shelf (Freitas et al., 2022). Moreover, elevated carbon flux may enhance benthic activity (Renaud et al., 2008), including bio-diffusion and bioirrigation that were also reported in the OS region

(Freitas et al., 2020), and may explain the near constant ^{210}Pb concentrations (Fig. 2). Therefore, although this area is under substantial ice cover during most of the year (Figure S1), changes in the primary productivity by Atlantification may shift OM export and leave signals within sediments biogeochemistry.

4.3.3. From the slope to the basin

Within the studied transect, the northern sites are more homogeneous than the southern sites regarding organic carbon content. The broad pattern in this slope to basin area is associated with high fine-grained sediment, water depth and sea ice concentration (Fig. 8). This is supported by ^{210}Pb deposition patterns. At the abyssal site NPAL19, the ^{210}Pb inventory is three times higher than on the shelf, and the surficial concentration ten times higher (Supplementary Table S2). This can be attributed to the longer water residence times and hence increased levels of enrichment of sediments deposited at these sites. The enrichment is due to continuous scavenging of ^{210}Pb$_{unsup}$ by settling particles and re-suspended sediment ^{210}Pb$_{unsup}$, which also can be available for scavenging (Sanchez-Cabeza et al., 1999). An additional factor affecting concentrations is the increased proportion of fine silts and clays at deeper sites (97.8 % <63 μm, Fig. 6). Since fine sediments typically have low settling velocities, they are likely to have travelled long distances before reaching the seabed (Elverhøi et al., 1989). Inputs of ^{210}Pb$_{unsup}$ to specific sites on the seabed will as a result have little relation to either the atmospheric flux at that locality, or production within the overlying water column.

These coupled environmental and spatial components are associated with low TOC and high TIC content (Fig. 8). Although the AW influenced shelf break station (P6) has been associated with seasonal high primary production and OM flux (Bodur et al., 2023), this region has low TOC$_{63}$ and is more similar with other sea ice-covered shelf stations despite also being distributed in the middle of the quadrant (Fig. 8). This pattern can be associated with the low sedimentation rates (NPAL15 Fig. 3) and lack of seasonality in the sediment parameters (P6, Fig. 5), thus, the organic carbon that is produced in this region might either be rapidly consumed or advected to other areas. While marine primary production is the main source of organic matter in the studied region (Morata and Renaud, 2008; Tamelander et al., 2008; Zaborska et al., 2008), the high ^{137}Cs inventories values on the northern slope (NPAL15, Table S2), far from continental sources, were previously attributed to melting ice cover (Zaborska et al., 2010). This suggests that at the deeper stations, the sediment and radionuclide deposition was partially derived from melting sea ice and may be associated with Svalbard glaciers and sediment-laden sea ice, which bring terrestrial particles from other Arctic shelves, such as the East Siberian Sea and the Laptev Sea (Elverhøi et al., 1989; Pfirman et al., 1990; Dowdeswell et al., 1998).

4.3.4. Carbonate content in the sediments

As in previous studies (e.g., Faust et al., 2020), there is an opposite distribution pattern between the total organic carbon and inorganic carbon content (Fig. 4). Sites north of the shelf break had the highest TIC values (equivalent to 10 % CaCO$_3$, Fig. 2), similar to values previously reported from the northern Svalbard shelf and slope (Stein et al., 1994) and higher than those measured near shallower shelf sites (Faust et al., 2020). High TIC values at slope and deeper areas (Fig. 8) are often associated with saline AW influx from the West Spitsbergen Current (Stein et al., 1994), however, the interplay between meltwater and AW alkalinity and dissolved inorganic carbon affects carbonate saturation, with seasonal variation (Chierici et al., 2019; Jones et al., 2023). Moreover, seasonal sea-ice processes and deep winter convection enhance the risk of acidification in deep waters over the shelf (Steinsund and Hald, 1994; Jones et al., 2023). Several studies described signs of dissolution in living calcareous benthic foraminifera in the Barents Sea shelf areas (e.g., stations A and B; Sjøblom, 2021), the southeast of Edgeøya (Fossile et al., 2020), and in the SW region (Steinsund and Hald, 1994). Dissolution of recently settled dead planktonic foraminifera was

also observed (Ofstad et al., 2021). Although the southern shelf region under AW domain is associated with high biological production and OM flux (Wexels Riser et al., 2008; Bodur et al., 2023), this is not reflected in the sedimentary TIC content (Figs. 2, 8). In the northern shelf, the metabolic dissolution of CaCO$_3$ resulting from aerobic degradation of organic matter leads to pH buffering of pore water and an increase in carbonate saturation in the sediments. In the southern sites, however, the low calcite content in the sediments does not reach a saturation state to allow carbonate precipitation (Freitas et al., 2022). Hence, the sedimentary inorganic carbon spatial variability is not only dependent on the *in situ* biological production but also to ice-ocean coupled processes that also affect acidification in the sediment compartment in the studied region.

4.4. Organic carbon accumulation

The average organic carbon accumulation rates (AR$_{toc}$) in the northern Barents Sea ranged from 1.7 to 13.4 g C$_{org}$ m^{-2} y^{-1} (top 10 cm, Fig. 6, Table 1). The slight increasing trend in AR$_{toc}$ since the late 1970 s may signal the steady increase in AW inflow and heat transport in the northern Barents Sea during the past decades (Ingvaldsen et al., 2021). Nonetheless, low down-core variation in TOC content resulted in low temporal variability in AR$_{toc}$, indicating a stable organic carbon content in the northern Barents Sea sediments for the past 100 years (Fig. 6). This observation agrees with findings of previous studies (Carroll et al., 2008a; Faust et al., 2021; Vare et al., 2010). In fact, the lack of temporal variability in most of the studied sedimentary parameters indicates that seasonal variations observed in the water column are not reflected in the multi-decadal sedimentary records. On continental shelves, the combined effect of well oxygenated bottom waters, low sedimentation rates, rapid consumption of fresh OM that reaches the seafloor, and enhanced bioturbation, contributes to high rates of OM degradation (Stein, 1990; Smeaton and Austin, 2022). In the Barents Sea, there is a high input of fresh organic matter to the benthos during spring, while more grazed material reaches the sediment during summer (Morata and Renaud, 2008; Bodur et al., 2023). The deposition of fresh detritus produces an almost immediate response in oxygen consumption (Morata et al., 2013), as benthic activity in the region is regulated by the amount and quality of organic matter that reaches the seafloor (Reigstad et al., 2011). Consequently, the organic matter reactivity changes most dramatically at the sediment–water interface where higher aerobic microbial activity is present but remains relatively unchanged across deeper sediment layers (Stevenson et al., 2020). While the processes that govern OM preservation in shelf sea sediments usually follow a water-depth and land-proximity gradient (i.e., high storage in inshore and coastal environments) (Smeaton and Austin, 2022), sea ice and water mass stratification in the Barents Sea also affect the OC flux to the seafloor and consequently the organic carbon accumulation. Although AR$_{toc}$ was not calculated in this study for high productive areas (e.g., Hopendypet, SW Olgastretet – Fig. 1, see Wexels Riser et al., 2008), other studies assert that these areas have AR$_{toc}$ associated with high SAR and biological production (Carroll et al., 2008a), which would result in higher preservation of organic carbon (Stein, 1990). In this sense, our results indicate that the low AR$_{toc}$ in the northern Barents Sea (Fig. 6) reflects long particle residence time as indicated by SAR (Fig. 3B) and possibly also due to rapid consumption of freshly deposited OM during bloom seasons on the uppermost layers of the sediment. Where the combined efficiency of microbial communities and benthic organisms in the utilization of labile and refractory carbon to energy production (Renaud et al., 2007) can result in only a small fraction of organic carbon accumulated and later buried in the sediments.

5. Conclusions and future prospects

Describing the spatial and temporal variability of geochemical components of marine sediments in the Barents Sea is challenging.

Generally, modern sedimentation on continental shelves is primarily influenced by water depth and land proximity, with nutrients and production decreasing towards deep-sea regions. In the northern Barents Sea, the irregular topography, as well as seasonal sea ice dynamics associated with the Atlantic Water (AW) inflow and mixing in two fronts increase the spatial variability in biogeochemical processes. Our results support the notion that sedimentation rate follows the water depth gradient of shelf, slope and basin, while it also is modulated by differences in particle size conditioned by the shelf topography. For example, shallower bank areas are sources of sediment and organic matter to depressions and troughs in surrounding areas. This is shown by the surface ^{210}Pb activity trends and grain size down-core distribution. Sea ice might also affect sediment deposition through particle import. In addition, there were no apparent seasonal differences in the analysed parameters and no substantial temporal variation in the sediment geochemical profiles. According to our results, the large-scale differences in organic carbon distribution are mainly linked to variations in sea ice concentration, water mass distribution and biological production, which confirms the presence of a biogeochemical separation between Arctic and Atlantic domains that corresponds with the Polar Front. We also identified a possible signal of north-eastward intrusion of AW into the northern Barents Sea in the biogeochemical properties in the SW Olgastretet. Furthermore, organic carbon accumulation rates in the northern Barents Sea reflect high degradation and particle residence time in the water column and sediment–water interface. Hence, any future changes induced by warming will likely affect the overall organic carbon distribution and accumulation, as well as its reactivity. Higher biological production only results in high OC accumulation if sedimentation rates also increase; thus, changes in the amount and quality of organic matter that reaches the seafloor would affect benthic community activity and structure before it leaves a record in OC accumulation rates. Therefore, additional knowledge about oxygen demand and carbon uptake by benthic communities, as well as changes in sediment transport by sea ice and bottom currents is important to understand how the factors that influence carbon flux and storage at larger scales will be affected by the changing climate. Moreover, more spatial surveys and intra-annual baseline estimates are necessary to address the uncertainties in how key environmental parameters affect biogeochemical dynamics in this complex sea floor environment.

CRediT authorship contribution statement

Thaise Ricardo de Freitas: Conceptualization, Data curation, Formal analysis, Investigation, Methodology, Visualization, Writing – original draft, Writing – review & editing. **Silvia Hess:** Conceptualization, Investigation, Methodology, Supervision, Validation, Writing – original draft. **Paul E. Renaud:** Supervision, Validation, Writing – review & editing. **Peter Appleby:** Methodology, Validation, Writing – review & editing. **Elisabeth Alve:** Conceptualization, Project administration, Resources, Validation, Writing – review & editing.

Declaration of competing interest

The authors declare that they have no known competing financial interests or personal relationships that could have appeared to influence the work reported in this paper.

Data availability

The datasets generated and analysed in this study were partially included in the Supplementary Material and deposited in the Norwegian Marine Data Centre (NMDC). This data is publicly available and can be found here: https://doi.org/10.21335/NMDC-1821375519, https://doi.org/10.21335/NMDC-350572235, https://doi.org/10.21335/NMDC-490057692, https://doi.org/10.21335/NMDC-799257283. The code for reproducing the plots and analyses is available in the GitHub repository.

Appendix A. Supplementary data

Supplementary data to this article can be found online at https://doi.org/10.1016/j.pocean.2024.103286.

References

Anglada-Ortiz, G., Meilland, J., Ziveri, P., Chierici, M., Fransson, A., Jones, E., et al., 2023. Seasonality of marine calcifiers in the northern Barents Sea: Spatiotemporal distribution of planktonic foraminifers and shelled pteropods and their contribution to carbon dynamics. Prog. Oceanogr. 218, 103121 https://doi.org/10.1016/j.pocean.2023.103121.

Appleby, P.G., 2004. Environmental change and atmospheric contamination on Svalbard: Sediment chronology. J. Paleolimnol. 31, 433–443. https://doi.org/10.1023/B:JOPL.0000022545.73163.ed.

Appleby, P., Nolan, P., Gifford, D., Godfrey, M., Oldfield, F., Anderson, N., et al., 1986. 210 pb dating by low background gamma counting. Hydrobiologia 143, 2127 b4sbjh.

Appleby, P.G., Oldfield, F., 1978. The calculation of lead-210 dates assuming a constant rate of supply of unsupported 210Pb to the sediment. Catena 5, 1–8 cjhj5h.

Appleby, P.G. (2001). "Chronostratigraphic Techniques in Recent Sediments," in, eds. W. M. Last and J. P. Smol (Dordrecht: Kluwer Academic Publishers), 171–203. doi: 10.1007/0-306-47669-X_9.

Årthun, M., Eldevik, T., Smedsrud, L.H., Skagseth, Ingvaldsen, R.B., 2012. Quantifying the influence of atlantic heat on Barents Sea ice variability and retreat. J. Clim. 25, 47364743 f34n39.

Athanase, M., Provost, C., Artana, C., Pérez-Hernández, M.D., Sennéchael, N., Bertosio, C., et al., 2021. Changes in atlantic water circulation patterns and volume transports north of svalbard over the last 12 years (2008–2020). J. Geophys. Res. Oceans 126, e2020JC016825 gmstj2.

Bauer, J.E., Cai, W.-J., Raymond, P.A., Bianchi, T.S., Hopkinson, C.S., Regnier, P.A.G., 2013. The changing carbon cycle of the coastal ocean. Nature 504, 61–70. https://doi.org/10.1038/nature12857.

Bodur, Y.V., Renaud, P.E., Goraguer, L., Amargant-Arumí, M., Assmy, P., Maria Dąbrowska, A., et al., 2023. Seasonal patterns of vertical flux in the northwestern Barents Sea under Atlantic Water influence and sea-ice decline. Prog. Oceanogr. 103132 https://doi.org/10.1016/j.pocean.2023.103132.

Borcard, D., Legendre, P., Drapeau, P., 1992. Partialling out the spatial component of ecological variation. Ecology 73, 1045–1055 c284tt.

Borcard, D., Gillet, F., Legendre, P., 2018. In: Numerical Ecology with R. Springer International Publishing, Cham. https://doi.org/10.1007/978-3-319-71404-2.

Carroll, M.L., Denisenko, S.G., Renaud, P.E., Ambrose, W.G., 2008b. Benthic infauna of the seasonally ice-covered western Barents Sea: Patterns and relationships to environmental forcing. Deep-Sea Res. Part II: Top. Stud. Oceanogr. 55, 23402351 c62qpb.

Carroll, J.L., Zaborska, A., Papucci, C., Schirone, A., Carroll, M.L., Pempkowiak, J., 2008a. Accumulation of organic carbon in western Barents Sea sediments. Deep-Sea Res. Part II: Top. Stud. Oceanogr. 55, 23612371 c6kgxq.

Chierici, M., Vernet, M., Fransson, A., Børsheim, K.Y., 2019. Net community production and carbon exchange from winter to summer in the Atlantic Water inflow to the Arctic Ocean. Front. Mar. Sci. 6 https://doi.org/10.3389/fmars.2019.00528.

Cochran, J.K., McKibbin-Vaughan, T., Dornblaser, M.M., Hirschberg, D., Livingston, H. D., Buesseler, K.O., 1990. 210Pb scavenging in the North Atlantic and North Pacific Oceans. Earth Planet. Sci. Lett. 97, 332–352 cmvm56.

DiGirolamo, N., Parkinson, C.L., Cavalieri, D.J., Gloersen, P., Zwally, H.J., 2023. Sea Ice Concentrations from Nimbus-7 SMMR and DMSP SSM/I-SSMIS Passive Microwave Data, Version 2. NASA National Snow and Ice Data Center Distributed Active Archive Center, Boulder, Colorado USA.

Dowdeswell, J.A., Elverhøi, A., Spielhagen, R.F., 1998. Glacimarine sedimentary processes and facies on the Polar North Atlantic margins. Quat. Sci. Rev. 17, 243272 cpch7c.

Dray, S., Bauman, D., Blanchet, G., Borcard, D., Clappe, S., Guenard, G., et al. (2021). *Adespatial: Multivariate multiscale spatial analysis*. Available at: https://CRAN.R-project.org/package=adespatial.

Dray, S., Pélissier, R., Couteron, P., Fortin, M.-J., Legendre, P., Peres-Neto, P.R., et al., 2012. Community ecology in the age of multivariate multiscale spatial analysis. Ecol. Monogr. 82, 257–275. https://doi.org/10.1890/11-1183.1.

Elverhøi, A., Pfirman, S.L., Solheim, A., Larssen, B.B., 1989. Glaciomarine sedimentation in epicontinental seas exemplified by the northern Barents Sea. Mar. Geol. 85, 225250 c36p56.

Erga, S.R., Ssebiyonga, N., Hamre, B., Frette, Ø., Rey, F., Drinkwater, K., 2014. Nutrients and phytoplankton biomass distribution and activity at the Barents Sea Polar Front during summer near Hopen and Storbanken. J. Mar. Syst. 130, 181–192. https://doi.org/10.1016/j.jmarsys.2012.12.008.

Falk-Petersen, S., Hop, H., Budgell, W.P., Hegseth, E.N., Korsnes, R., Løyning, T.B., et al., 2000. Physical and ecological processes in the marginal ice zone of the northern Barents Sea during the summer melt period. J. Mar. Syst. 27, 131159 dxbxh7.

Faust, J., Stevenson, M., Abbott, G., Knies, J., Tessin, A., Mannion, I., et al., 2020. Does Arctic warming reduce preservation of organic matter in Barents Sea sediments? Philos. Trans. R. Soc. A Math. Phys. Eng. Sci. gkdcqd.

Faust, J.C., Tessin, A., Fisher, B.J., Zindorf, M., Papadaki, S., Hendry, K.R., et al., 2021. Millennial scale persistence of organic carbon bound to iron in Arctic marine sediments. Nat. Commun. 12, 275 ghstng.

Fennel, K., Alin, S., Barbero, L., Evans, W., Bourgeois, T., Cooley, S., et al., 2019. Carbon cycling in the North American coastal ocean: A synthesis. Biogeosciences 16, 1281–1304. https://doi.org/10.5194/bg-16-1281-2019.

Fetterer, F., Knowles, K., Meier, W.N., Savoie, M., Windnagel, A.K. (2017). Sea Ice Index, Version 3. doi: 10.7265/N5K072F8.

Fossile, E., Pia Nardelli, M., Jouini, A., Lansard, B., Pusceddu, A., Moccia, D., et al., 2020. Benthic foraminifera as tracers of brine production in Storfjorden sea ice factory. Biogeosciences 17, 19331953. https://doi.org/10.5194/bg-2019-405.

Freitas, F.S., Hendry, K.R., Henley, S.F., Faust, J.C., Tessin, A.C., Stevenson, M.A., et al., 2020. Benthic-pelagic coupling in the Barents Sea: An integrated data-model framework. Philos. Transact. A Math. Phys. Eng. Sci. 378, 20190359 gkdcqc.

Freitas, F.S., Arndt, S., Hendry, K.R., Faust, J.C., Tessin, A.C., März, C., 2022. Benthic organic matter transformation drives pH and carbonate chemistry in Arctic marine sediments. Global Biogeochem. Cycles, e2021GB007187. https://doi.org/10.1029/2021GB007187.

Gerland, Sebastian (2022). CTD data from Nansen Legacy cruise - Seasonal Cruise Q1. doi: 10.21335/NMDC-1491279668.

Harrison, W.G., Cota, G.F., 1991. Primary production in polar waters: Relation to nutrient availability. Polar Res. 10, 87–104 gkdcp8.

Husum, K., Ninnemann, U., Rydningen, T.A., Alve, E., Altuna, N.E.B., Braaten, A.H., et al., 2020. Paleo Cruise 2018. NLRS. https://doi.org/10.7557/nlrs.5502.

Husum, Katrine (2022). CTD data from Nansen Legacy cruise - Paleo Cruise. doi: 10.21335/NMDC-63841658.

Ingvaldsen, R.B., Assmann, K.M., Primicerio, R., Fossheim, M., Polyakov, I.V., Dolgov, A. V., 2021. Physical manifestations and ecological implications of Arctic Atlantification. Nat. Rev. Earth Environ. 2, 874–889. https://doi.org/10.1038/s43017-021-00228-x.

Jakobsson, M., Mayer, L.A., Bringensparr, C., Castro, C.F., Mohammad, R., Johnson, P., et al., 2020. The international bathymetric chart of the Arctic Ocean Version 4.0. Sci. Data 7, 176 doi: gjdsg2.

Jones, E.M., Chierici, M., Fransson, A., Assmann, K.M., Renner, H.H., Hodal Lødemel, H., 2023. Inorganic carbon and nutrient dynamics in the marginal ice zone of the Barents Sea: Seasonality and implications for ocean acidification. Prog. Oceanogr. 219, 103131 https://doi.org/10.1016/j.pocean.2023.

Kim, H., Kwon, S.Y., Lee, K., Lim, D., Han, S., Kim, T.W., et al., 2020. Input of terrestrial organic matter linked to deglaciation increased mercury transport to the Svalbard fjords. Sci. Rep. 10, 3446 gkdfpm.

Knies, J., Martinez, P., 2009. Organic matter sedimentation in the western Barents Sea region: Terrestrial and marine contribution based on isotopic composition and organic nitrogen content. Nor. J. Geol. 89, 7989.

Lannuzel, D., Tedesco, L., van Leeuwe, M., Campbell, K., Flores, H., Delille, B., et al., 2020. The future of Arctic sea-ice biogeochemistry and ice-associated ecosystems. Nat. Clim. Chang. 10, 983–992 ghmvhj.

Laruelle, G.G., Lauerwald, R., Pfeil, B., Regnier, P., 2014. Regionalized global budget of the CO_2 exchange at the air-water interface in continental shelf seas. Global Biogeochem. Cycles 28, 1199–1214. https://doi.org/10.1002/2014GB004832.

Laruelle, G.G., Cai, W.-J., Hu, X., Gruber, N., Mackenzie, F.T., Regnier, P., 2018. Continental shelves as a variable but increasing global sink for atmospheric carbon dioxide. Nat. Commun. 9, 454. https://doi.org/10.1038/s41467-017-02738-z.

Lien, V.S., Trofimov, A.G., 2013. Formation of Barents Sea Branch Water in the north-eastern Barents Sea. Polar Res. 32, 18905 gbdwd3.

Lind, S., Ingvaldsen, R.B., 2012. Variability and impacts of Atlantic Water entering the Barents Sea from the north. Deep Sea Res. Part I 62, 70–88 fxkxvx.

Lind, S., Ingvaldsen, R.B., Furevik, T., 2018. Arctic warming hotspot in the northern Barents Sea linked to declining sea-ice import. Nat. Clim. Chang. 8, 634639 crfh.

Loeng, H., 1991. Features of the physical oceanographic conditions of the Barents Sea. Polar Res. 10, 518 gkdcpx.

Ludvigsen, Martin (2022). CTD data from Nansen Legacy cruise - Seasonal Cruise Q2. doi: 10.21335/NMDC-515075317.

Lundesgaard, Ø., Sundfjord, A., Lind, S., Nilsen, F., Renner, 2022. Import of Atlantic Water and sea ice controls the ocean environment in the northern Barents Sea. Ocean Sci. 18, 1389–1418. https://doi.org/10.5194/os-18-1389-2022.

Maiti, K., Carroll, J.L., Benitez-Nelson, C.R., 2010. Sedimentation and particle dynamics in the seasonal ice zone of the Barents Sea. J. Mar. Syst. 79, 185198 bknc8v.

Midttun, L., 1985. Formation of dense bottom water in the Barents Sea. Deep Sea Res. Part A 32, 12331241 c8c4wp.

Morata, N., Michaud, E., Włodarska-Kowalczuk, M., 2013. Impact of early food input on the Arctic benthos activities during the polar night. Polar Biol. 38, 99114 f6w8m7.

Morata, N., Renaud, P.E., 2008. Sedimentary pigments in the western Barents Sea: A reflection of pelagic-benthic coupling? Deep-Sea Res. Part II: Top. Stud. Oceanogr. 55, 23812389 cx3bs2.

Nöthig, Eva-Maria; Petersen, Imke; Schröter, Franz; Lorenzen, Christiane (2018): Chlorophyll a measured on water bottle samples during POLARSTERN cruise PS94 (ARK-XXIX/3). Alfred Wegener Institute, Helmholtz Centre for Polar and Marine Research, Bremerhaven, PANGAEA, https://doi.org/10.1594/PANGAEA.887934.

Nürnberg, D., Levitan, M.A., Pavlidis, J.A., Shelekhova, E.S., 1995. Distribution of clay minerals in surface sediments from the eastern Barents and south-western Kara seas. Geol. Rundsch. 84 fjb2ff.

Ofstad, S., Zamelczyk, K., Kimoto, K., Chierici, M., Fransson, A., Rasmussen, T.L., 2021. Shell density of planktonic foraminifera and pteropod species *Limacina helicina* in the Barents Sea: Relation to ontogeny and water chemistry. PLoS One 16, e0249178.

Oldfield, F., Appleby, P.G., 1984. A combined radiometric and mineral magnetic approach to recent geochronology in lakes affected by catchment disturbance and sediment redistribution. Chem. Geol. 44, 67–83. https://doi.org/10.1016/0009-2541(84)90067-6.

Oleszczuk, B., Michaud, E., Morata, N., Renaud, P.E., Kędra, M., 2019. Benthic macrofaunal bioturbation activities from shelf to deep basin in spring to summer transition in the Arctic Ocean. Mar. Environ. Res. 150, 104746 gkdcpn.

Paradis, S., Puig, P., Masqué, P., Juan-Díaz, X., Martín, J., Palanques, A., 2017. Bottom-trawling along submarine canyons impacts deep sedimentary regimes. Sci. Rep. 7, 43332. https://doi.org/10.1038/srep43332.

Pathirana, I., Knies, J., Felix, M., Mann, U., Ellingsen, I., 2015. Middle to late Holocene paleoproductivity reconstructions for the western Barents Sea: A model-data comparison. Arktos 1, 117 gkdcwj.

Pfirman, S., Lange, M.A., Wollenburg, I., Schlosser, P. (1990). "Sea ice characteristics and the role of sediment inclusions in deep-sea deposition: Arctic - Antarctic comparisons," in (Dordrecht: Springer Netherlands), 187211. doi: 10.1007/978-94-009-2029-3_11.

Pfirman, S.L., Bauch, D., Gammelsrød, T. (1994). "The northern Barents Sea: Water mass distribution and modification," in, eds. 0. M. Johannessen, R. D. Muench, and J. E. Overland, 7794. doi: 10.1029/gm085p0077.

R Core Team, 2020. R: A language and environment for statistical computing. R Foundation for Statistical Computing, Vienna, Austria. Available at: http://www.R-project.org/.

Rachold, V., Eicken, H., Gordeev, V.V., Grigoriev, M.N., Hubberten, H.-W., Lisitzin, A.P., et al. (2004). "Modern terrigenous organic carbon input to the Arctic Ocean," in, eds. R. Stein and R. W. MacDonald (Berlin, Heidelberg: Springer), 33–55. doi: 10.1007/978-3-642-18912-8_2.

Reigstad, M., Carroll, J., Slagstad, D., Ellingsen, I., Wassmann, P., 2011. Intra-regional comparison of productivity, carbon flux and ecosystem composition within the northern Barents Sea. Prog. Oceanogr. 90, 33–46. https://doi.org/10.1016/j.pocean.2011.02.005.

Reigstad, Marit (2022). CTD data from Nansen Legacy cruise - Seasonal Cruise Q3. doi: 10.21335/NMDC-1107597377.

Renaud, P.E., Riedel, A., Michel, C., Morata, N., Gosselin, M., Juul-Pedersen, T., et al., 2007. Seasonal variation in benthic community oxygen demand: A response to an ice algal bloom in the Beaufort Sea, Canadian Arctic? J. Mar. Syst. 67, 112 bkxktd.

Renaud, P.E., Morata, N., Carroll, M.L., Denisenko, S.G., Reigstad, M., 2008. Pelagic-benthic coupling in the western Barents Sea: Processes and time scales. Deep-Sea Res. Part II: Top. Stud. Oceanogr. 55, 23722380 fnv9gg.

Sanchez-Cabeza, J.A., Masqué, P., Ani-Ragolta, I., Merino, J., Frignani, M., Alvisi, F., et al., 1999. Sediment accumulation rates in the southern Barcelona continental margin (NW Mediterranean Sea) derived from 210Pb and 137Cs chronology. Prog. Oceanogr. 44, 313–332. https://doi.org/10.1016/S0079-6611(99)00031-2.

Sjøblom, M.A.N. (2021). Environmental changes in the Barents Sea – Does the invasive snow crab disturb the sediment and geochemical composition in the Barents Sea? [dissertation/master's thesis]. Available at: https://www.duo.uio.no/handle/10852/89245 [Accessed April 11, 2022].

Smeaton, C., Austin, W., 2022. Quality not quantity: Prioritizing the management of sedimentary organic matter across continental shelf seas. Geophys. Res. Lett. https://doi.org/10.1029/2021GL097481.

Smith, J.N., Ellis, K.M., Naes, K., Dahle, S., Matishov, D., 1995. Sedimentation and mixing rates of radionuclides in Barents Sea sediments off Novaya Zemlya. Deep Sea Res. Part II 42, 1471–1493 bt7stk.

Solan, M., Ward, E.R., Wood, C.L., Reed, A.J., Grange, L.J., Godbold, J.A., 2020. Climate-driven benthic invertebrate activity and biogeochemical functioning across the Barents Sea polar front. Philos. Transact. A Math. Phys. Eng. Sci. 378, 20190365 gkdcqv.

Søreide, Janne (2022). CTD data from Nansen Legacy cruise - Seasonal Cruise Q4. doi: 10.21335/NMDC-301551919.

Stein, R., 1990. Organic carbon content/sedimentation rate relationship and its paleoenvironmental significance for marine sediments. Geo-Mar. Lett. 10, 37–44. https://doi.org/10.1007/BF02431020.

Stein, R., Grobe, H., Wahsner, M., 1994. Organic carbon, carbonate, and clay mineral distributions in eastern central Arctic Ocean surface sediments. Mar. Geol. 119, 269–285. https://doi.org/10.1016/0025-3227(94)90185-6.

Steinsund, P.I., Hald, M., 1994. Recent calcium carbonate dissolution in the Barents Sea: Paleoceanographic applications. Mar. Geol. 117, 303316 fd6dq7.

Sternberg, R.W., Aagaard, K., Cacchione, D., Wheatcroft, R.A., Beach, R.A., Roach, A.T., et al., 2001. Long-term near-bed observations of velocity and hydrographic properties in the northwest Barents Sea with implications for sediment transport. Cont. Shelf Res. 21, 509529 fp9dvv.

Stevenson, M.A., Abbott, G.D., 2019. Exploring the composition of macromolecular organic matter in arctic ocean sediments under a changing sea ice gradient. J. Anal. Appl. Pyrol. 140, 102111 gkdcqs.

Stevenson, M.A., Faust, J.C., Andrade, L.L., Freitas, F.S., Gray, N.D., Tait, K., et al., 2020. Transformation of organic matter in a Barents Sea sediment profile: Coupled geochemical and microbiological processes. Philos. Transact. A Math. Phys. Eng. Sci. 378, 20200223 ghvq55.

Strass, V.H., Niithig, E.-M., 1996. Seasonal shifts in ice edge phytoplankton blooms in the Barents Sea related to the water column stability. Polar Biol. 16, 409–422. https://doi.org/10.1007/BF02390423.

Stumpf, R. P. (2009). Distance to Nearest Coastline: 0.01-Degree Grid. NASA Ocean Biology Processing Group; NASA Goddard Space Flight Center. Available at: https://oceancolor.gsfc.nasa.gov/resources/docs/distfromcoast/ (Accessed August 19, 2021).

Tamelander, T., Reigstad, M., Hop, H., Carroll, M.L., Wassmann, P., 2008. Pelagic and sympagic contribution of organic matter to zooplankton and vertical export in the Barents Sea marginal ice zone. Deep Sea Res. Part II 55, 2330–2339. https://doi.org/10.1016/j.dsr2.2008.05.019.

Vader, A. (2022). Chlorophyll A and phaeopigments Nansen Legacy. https://doi.org/10.21335/NMDC-1371694848.

Veileder (2018). Klassifiseringsveileder 02:2018 Klassifisering av miljøtilstand i vann. Økologisk og kjemisk klassifiseringssystem for kystvann, grunnvann, innsjøer og elver. Available at: https://www.vannportalen.no/veiledere/klassifiseringsveileder/.

Vare, L.L., Massé, G., Belt, S.T., 2010. A biomarker-based reconstruction of sea ice conditions for the Barents Sea in recent centuries. The Holocene 20, 637–643. https://doi.org/10.1177/0959683609355179.

Vogt, C., Knies, J., 2009. Sediment pathways in the western Barents Sea inferred from clay mineral assemblages in surface sediments. Nor. J. Geol. 89, 41–55.

Wexels Riser, C., Wassmann, P., Reigstad, M., Seuthe, L., 2008. Vertical flux regulation by zooplankton in the northern Barents Sea during Arctic spring. Deep Sea Res. Part II 55, 2320–2329. https://doi.org/10.1016/j.dsr2.2008.05.006.

Wiedmann, I., Ershova, E., Bluhm, B.A., Nöthig, E.M., Gradinger, R.R., Kosobokova, K., et al., 2020. What feeds the benthos in the Arctic basins? Assembling a carbon budget for the deep Arctic Ocean. Front. Mar. Sci. 7 gkdcqn.

Winkelmann, D., Knies, J., 2005. Recent distribution and accumulation of organic carbon on the continental margin west off Spitsbergen. Geochem. Geophys. Geosyst. 6 b5qpmm.

Wood, S. N. (2017). *Generalized Additive Models: An Introduction with R.* 2nd ed. Chapman; Hall/CRC doi: 10.1201/9781315370279.

Yasunaka, S., Siswanto, E., Olsen, A., Hoppema, M., Watanabe, E., Fransson, A., et al., 2018. Arctic Ocean CO_2 uptake: An improved multiyear estimate of the air-sea CO_2 flux incorporating chlorophyll *a* concentrations. Biogeosciences 15, 1643–1661. https://doi.org/10.5194/bg-15-1643-2018.

Zaborska, A., Carroll, J.L., Papucci, C., Torricelli, L., Carroll, M.L., Walkusz-Miotk, J., et al., 2008. Recent sediment accumulation rates for the western margin of the Barents Sea. Deep-Sea Res. Part II: Top. Stud. Oceanogr. 55, 23522360 dsqm8b.

Zaborska, A., Mietelski, J.W., Carroll, J., Papucci, C., Pempkowiak, J., 2010. Sources and distributions of 137Cs, 238Pu, 239,240Pu radionuclides in the north-western Barents Sea. J. Environ. Radioact. 101, 323–331, 10/bnngz7.